

Spatial Structure and Collisionless Electron Heating in Balmer-dominated Shocks

Matthew van Adelsberg¹, Kevin Heng², Richard McCray¹, John C. Raymond³

ABSTRACT

Balmer-dominated shocks in supernova remnants (SNRs) produce strong hydrogen lines with a two-component profile composed of a narrow contribution from cold upstream hydrogen atoms, and a broad contribution from hydrogen atoms that have undergone charge transfer reactions with hot protons. Observations of emission lines from edge-wise shocks in SNRs can constrain the gas velocity and collisionless electron heating at the shock front. Downstream hydrogen atoms engage in charge transfer, excitation and ionization reactions, defining an interaction region called the shock transition zone, with characteristic width $l_{\text{zone}} \sim 10^{15}$ cm, for shock velocity $v_s \sim 1000$ km s⁻¹ and upstream density $n_0 \sim 1$ cm⁻³. The properties of hot hydrogen atoms undergoing charge transfer (called broad neutrals) are critical for accurately calculating the structure and radiation from the shock transition zone. This paper is the third in a series describing the kinetic, fluid and emission properties of Balmer-dominated shocks, and is the first to treat properly the effect of broad neutral kinetics on shock transition zone structure. We use our models to extract shock parameters from observations of Balmer-dominated SNRs. We find that inferred shock velocities and electron temperatures are systematically lower (by $\sim 30-50\%$) than those of previous calculations. Our results have a strong dependence on the ratio of electron to proton temperatures, $\beta \equiv T_e/T_p$. We construct a relation $\beta(v_s)$ between the temperature ratio and shock velocity and show that post-shock electrons are heated to higher temperatures at larger shock velocities, contrary to the velocity independent heating mechanism proposed by Ghavamian et al. (2007b).

Subject headings: shock waves — supernova remnants

¹JILA, University of Colorado, 440 UCB, Boulder, CO 80309; mvanadel@jilau1.colorado.edu

²Institute for Advanced Study, Einstein Drive, Princeton, NJ 08540

³Harvard-Smithsonian Center for Astrophysics, 60 Garden Street, Cambridge, MA 02138

1. Introduction

Balmer-dominated shocks in supernova remnants (SNRs) encounter upstream gas containing a substantial fraction of neutral hydrogen atoms. Emission from the shock is characterized by strong Balmer and Lyman lines with two-component profiles, consisting of a narrow contribution from direct excitation of the hydrogen atoms entering the shock, and a broad contribution from excitation of “broad neutrals,” hydrogen atoms that have been produced by charge transfer reactions with protons in the downstream gas (Chevalier & Raymond 1978; Chevalier et al. 1980). Such shocks are seen in many SNRs, including parts of the Cygnus Loop (Ghavamian et al. 2001, hereafter G01), Tycho and Kepler’s remnants (Kirshner et al. 1987, KCW87a; Smith et al. 1991, S91; G01; Fesen et al. 1989, F89), RCW 86 (G01; Ghavamian et al. 2007b, G07b), SN 1006 (KCW87; S91; Ghavamian et al. 2002, G02), and several remnants located in the LMC (Tuohy et al. 1982, T82; S91; Ghavamian et al. 2003, G03; Ghavamian et al. 2007a, G07a).

By observing profiles of broad emission lines from shocks seen edge-wise in SNRs, one can infer their velocities, which can then be compared to observations of proper motion to infer distances to the objects (Chevalier et al. 1980; Kirshner et al. 1987). Observations which resolve the spatial profile of the combined $H\alpha$ emission can constrain the neutral fraction and density of the upstream gas (Raymond et al. 2007).

In addition to diagnosing parameters of SNRs, Balmer-dominated shocks provide an important probe into the plasma physics of collisionless, non-relativistic shocks. Models of the width of the broad line and integrated intensity ratio of the broad-to-narrow components can be used to derive the ratio of electron to proton temperature as a function of shock velocity. Such a curve can provide insight into the physical mechanisms at work in the shocked plasma.

This is the third in a series of papers investigating the hydrodynamics, kinetics, and line emission from Balmer-dominated shocks. In Heng & McCray 2007 (Paper 1), we calculated distribution functions for hydrogen atoms engaging in charge transfer reactions with hot protons, and computed the ratio of broad-to-narrow line emission as a function of shock velocity. In Heng et al. 2007 (Paper 2) we calculated the density structure of the shock transition zone, where hydrogen atoms passing the shock front undergo charge transfer reactions, emit radiation, and become fully ionized.

The approximations employed in Paper 2 limit the validity of the results to shocks entering the upstream gas with velocities ($< 3000 \text{ km s}^{-1}$), due to our treatment of the broad neutrals as a single fluid with the same bulk velocity as the ions (our “restricted three-component model”). In fact, the broad neutrals in the shock transition region are not

a fluid, but have distinct anisotropic distribution functions depending on how many charge transfer reactions they have undergone (Paper 1). In the present paper, we treat charged species in the shocked gas as fluids, and describe the hydrogen atoms with appropriate kinetic distribution functions. In addition, we provide an improved calculation of the broad emission line velocity profile. With the methodology described here, we can calculate the structure of the shock transition zone more accurately and characterize hydrogen line emission from shocks with $v_s \sim 300 - 10,000 \text{ km s}^{-1}$. Moreover, we can calculate the emission line profiles and component ratios with greater accuracy than before.

Our results imply lower values of the inferred shock velocity and proton-electron temperature equilibration than those found from previous models. We find that we can self-consistently determine these parameters for most Balmer-dominated SNRs. For at least one SNR, however, the basic model must be augmented by new physics to account for observations. In addition, our work has implications for the validity of shock velocity estimates for several SNRs, including the Cygnus loop. We also infer a dependence of collisionless electron heating on shock velocity which differs from that proposed by Ghavamian et al. (2007b).

In §2 of this paper, we describe our physical model. In §3, we display the equations employed to calculate the structure of the shock transition zone and describe our numerical solution. In §4, we show how to calculate the spatial emission profile from the shock transition zone and line spectra of hydrogen. In §5, we analyze our results and describe how observations of Balmer-dominated SNRs should be interpreted in light of our new model. Finally, in §6, we discuss implications of our results for collisionless electron heating, limitations of our model, and highlight areas for future research.

2. Physical Model

We consider a shock with velocity $v_s \gtrsim 300 - 10,000 \text{ km s}^{-1}$ traveling through the ISM, which consists of cold, partially neutral hydrogen and neutral helium. The pre-shock fraction of helium, relative to hydrogen, is denoted f_{He} . If the total upstream density of protons and hydrogen atoms is n_0 , then the fraction of pre-shock protons is defined to be $f_p = n_p/n_0$.

In the frame of the shock, the cold upstream neutrals and charged particles flow downstream with uniform velocity v_s . At the shock, we assume that the protons are heated in a thermal distribution to $T_p \sim \frac{3m_p v_s^2}{16k_B} \sim 10^7 \text{ K}$ for $v_s \sim 10^8 \text{ cm s}^{-1}$. At the high post-shock temperatures in Balmer-dominated remnants, emission from hydrogen excitation is much stronger than forbidden transitions in metals seen in other galactic nebulae (e.g., Shull & McKee 1979). The length scale for thermalization of protons is set by the proton

cyclotron gyroradius, $l_{\text{gyro}} \sim 10^8$ cm at $B \sim 10^{-4}$ G, which is much less than the length scale for the shock transition zone, $l_{\text{zone}} \sim 1/(n_0\sigma) = 10^{15}$ cm, which is set by the mean-free paths for excitation, charge transfer and ionization reactions.

Without any energy transfer between shocked protons and shocked electrons, the temperature of the electrons is expected to be a factor of m_e/m_p less than that of the protons. Since the collisional timescale for temperature equilibration between electrons and protons is longer than the age of the remnant (e.g., Spitzer 1962), the electrons will remain at a fixed temperature with respect to the protons in the downstream material. However, several authors have argued that electromagnetic instabilities at the shock front can increase the electron temperature, with estimates ranging from $T_e \sim 0.1T_p$ to complete equilibration (see Cargill & Papadopoulos 1988; Vink et al. 2003; Mikhailovskii 1992; Ghavamian et al. 2007b, and the references therein). Since the physics of non-relativistic, collisionless shocks is still poorly understood, we parametrize the electron temperature using the definition

$$\beta \equiv \frac{T_e}{T_p}. \quad (1)$$

One of the goals of our work is to use observations of Balmer-dominated remnants to constrain the value of β in the shock transition zone as a function of shock velocity.

Negligible interactions take place between neutral and charged species in the upstream gas. The cold neutral hydrogen atoms passing through the shock are not affected by the discontinuity. In contrast, the bulk velocity of the downstream thermal protons and electrons becomes approximately $v_s/4$, at which point ionization and charge transfer reactions between cold atoms and hot protons occur (see §5.1). These reactions produce a new population of hot atoms, referred to as broad neutrals.¹ The H α emission is produced by charge transfer to excited states and excitation reactions in the shock transition zone. The narrow and broad components of the line are emitted by the cold hydrogen and broad neutrals, respectively.

The spatial and velocity distributions of the broad neutrals are critical for calculating the correct structure and emission from the transition zone. In Paper 2, we assumed that the broad neutrals could be characterized as a single fluid, with velocity and temperature equal to that of the ions. This treatment is flawed because, unlike the ionic species, the broad neutrals have negligible interactions among themselves. Therefore, each time a neutral engages in charge exchange, it becomes part of a new distribution with distinct velocity and

¹Initially, the reaction will produce a cold proton, which is re-energized through Coloumb collisions with the hot proton population and gyro motion around the magnetic field, processes which occur over a much smaller length scale than the atom-ion interactions. Thus, the proton is quickly subsumed into the thermal population.

temperature (see Paper 1), which is not subsumed by the original population. This fact has not, until now, been properly taken into account in the literature.

The detailed kinetic properties of the particle distributions and their reaction rates were calculated in Paper 1. We use those results in our fluid treatment of the shock transition zone structure below. In this picture, the broad neutrals form an infinite set of atomic populations with distinct reaction rates. In practice, as noted in Paper 1, the velocity distribution function of atoms experiencing many charge transfers rapidly converges to that of the protons, usually after only three or more interactions. Thus, there are effectively only three distinct broad components which interact with the other species. The bulk velocities and temperatures of the broad components are written:

$$v_k = F_{v,k} v_p, \quad (2)$$

$$T_k = F_{T,k} T_p, \quad (3)$$

where v_k and T_k are the velocity and temperature of a broad neutral population after k charge transfers. The coefficients $F_{v,k}(v_s, \beta, f_p, f_{He})$ and $F_{T,k}(v_s, \beta, f_p, f_{He})$ are calculated using the methods described in Paper 1 and, in principle, are also functions of v_p and T_p . However, we show in §5.1 that the proton velocity and temperature do not vary significantly enough in the shock transition zone to affect the values of these coefficients. For $k \geq 3$, $F_{v,k}$ and $F_{T,k}$ are taken to be unity.

Ionization of helium in the shock transition zone produces singly-ionized He^+ and alpha particles. We assume that these ions flow with the same velocity as the proton and electron fluids. Figure 1 displays schematically the density variation of the different particle species in the shock transition zone.

3. Spatial Structure of the Transition Zone

3.1. Basic Equations

We employ a plane-parallel coordinate system in the frame of the shock, in which the shock front is at $z = 0$. The density structure of the transition zone is determined by conservation of mass flux:

$$\frac{d}{dz} n_H = -n_H \sum_{s=e}^{\alpha} n_s \tilde{R}_{iH,s} - n_H n_p \tilde{R}_{T0,p}, \quad (4)$$

$$\frac{d}{dz} (n_1 v_1) = n_H n_p \tilde{R}_{T0,p} - n_1 \sum_{s=e}^{\alpha} n_s \tilde{R}_{iB,s} - n_1 n_p \tilde{R}_{T,p}, \quad (5)$$

$$\frac{d}{dz}(n_2 v_2) = n_1 n_p \tilde{R}_{T,p} - n_2 \sum_{s=e}^{\alpha} n_s \tilde{R}_{iB,s} - n_2 n_p \tilde{R}_{T,p}, \quad (6)$$

$$\vdots$$

$$\frac{d}{dz}(n_k v_k) = n_{k-1} n_p \tilde{R}_{T,p} - n_k \sum_{s=e}^{\alpha} n_s \tilde{R}_{iB,s} - n_k n_p \tilde{R}_{T,p}, \quad (7)$$

$$\vdots$$

$$\frac{d}{dz} n_{He} = -n_{He} \sum_{s=e}^{\alpha} n_s \tilde{R}_{iHe,s}, \quad (8)$$

$$\frac{d}{dz}(n_{He^+} v_i) = n_{He} \sum_{s=e}^{\alpha} n_s \tilde{R}_{iHe,s} - n_{He^+} \sum_{s=e}^{\alpha} n_s \tilde{R}_{iHe^+,s}, \quad (9)$$

$$\frac{d}{dz}(n_{\alpha} v_i) = n_{He^+} \sum_{s=e}^{\alpha} n_s \tilde{R}_{iHe^+,s}, \quad (10)$$

$$\frac{d}{dz}(n_p v_i) = \sum_{s=e}^{\alpha} n_s \left(n_H \tilde{R}_{iH,s} + \sum_{k=1}^N n_k \tilde{R}_{iB,s} \right), \quad (11)$$

where the rate coefficients \tilde{R} for the atomic interactions are defined in Paper 1. Charge conservation requires the electron density to obey the relation $n_e = n_p + n_{He^+} + 2n_{\alpha}$. The subscripts iH , iHe , and iHe^+ denote ionization of hydrogen, helium, and singly-ionized helium, while the index s runs over the charged particles $s = \{e, p, He^+, \alpha\}$ (electrons, protons, singly-ionized helium and alpha particles) participating in the reactions. The subscript T_0 indicates charge transfer of cold hydrogen atoms with protons. While each broad population will have a separate rate coefficient for each atomic interaction, in practice, the values are not sensitive to the details of the broad distribution functions. Therefore, we use one rate coefficient to describe all the broad populations: the subscripts iB and T denote ionization and charge transfer, respectively. We list the references for our interaction cross sections and rate coefficients in Appendix A.

The system of differential equations is completed by expressions for conservation of momentum and energy flux:

$$\frac{d}{dz} \left[n_H + \sum_{k=1}^{\infty} (P_k + n_k v_k^2) + n_{He} + \sum_{s=e}^{\alpha} (P_s + n_s v_i^2) \right] = 0, \quad (12)$$

$$\frac{d}{dz} \left[n_H + \sum_{k=1}^{\infty} (P_k + U_k + n_k v_k^2) v_k + n_{He} + \sum_{s=e}^{\alpha} (P_s + U_s + n_s v_i^2) v_i \right] = 0, \quad (13)$$

where $P = nk_B T$ is the pressure and $U = \frac{3}{2}nk_B T$ is the energy density.

We define a natural length scale for the transition zone, according to the formula:

$$l_z \equiv \frac{v_s}{n_0 \bar{R}}, \quad (14)$$

where \bar{R} is a typical value for the interaction rate coefficients, taken to be $10^{-8} \text{ cm}^3 \text{ s}^{-1}$. We also define a set of dimensionless variables with $\chi \equiv z/l_z$, $\eta \equiv n/n_0$, $u \equiv v/v_s$, and $\epsilon \equiv k_B T/(m_p v_s^2)$. As discussed above, broad neutrals which have engaged in three or more charge transfers can be described with the thermal proton distribution function. We therefore define $\eta_N = \sum_{k=3}^{\infty} \eta_k$. Summing over eqs. (7) with $k \geq 3$ and using these definitions, the formulas for the shock transition zone structure can be written:

$$\frac{d}{d\chi} \eta_H = -\eta_H \sum_{s=e}^{\alpha} \eta_s \mathcal{R}_{iH,s} - \eta_H \eta_p \mathcal{R}_{T_0,p}, \quad (15)$$

$$\frac{d}{d\chi} (\eta_1 u_1) = \eta_H \eta_p \mathcal{R}_{T_0,p} - \eta_1 \sum_{s=e}^{\alpha} \eta_s \mathcal{R}_{iB,s} - \eta_1 \eta_p \mathcal{R}_{T,p}, \quad (16)$$

$$\frac{d}{d\chi} (\eta_2 u_2) = \eta_1 \eta_p \mathcal{R}_{T,p} - \eta_2 \sum_{s=e}^{\alpha} \eta_s \mathcal{R}_{iB,s} - \eta_2 \eta_p \mathcal{R}_{T,p}, \quad (17)$$

$$\frac{d}{d\chi} (\eta_N u_i) = \eta_2 \eta_p \mathcal{R}_{T,p} - \eta_N \sum_{s=e}^{\alpha} \eta_s \mathcal{R}_{iB,s}, \quad (18)$$

$$\frac{d}{d\chi} \eta_{He} = -\eta_{He} \sum_{s=e}^{\alpha} \eta_s \mathcal{R}_{iHe,s}, \quad (19)$$

$$\frac{d}{d\chi} (\eta_{He^+} u_i) = \eta_{He} \sum_{s=e}^{\alpha} \eta_s \mathcal{R}_{iHe,s} - \eta_{He^+} \sum_{s=e}^{\alpha} \eta_s \mathcal{R}_{iHe^+,s}, \quad (20)$$

$$\frac{d}{d\chi} (\eta_{\alpha} u_i) = \eta_{He^+} \sum_{s=e}^{\alpha} \eta_s \mathcal{R}_{iHe^+,s}, \quad (21)$$

$$\frac{d}{d\chi} (\eta_p u_i) = \sum_{s=e}^{\alpha} \eta_p \left(\eta_H \mathcal{R}_{iH,s} + \sum_{s=e}^{\alpha} \eta_k \mathcal{R}_{iB,s} \right), \quad (22)$$

$$\frac{d}{d\chi} \left[\eta_H + \sum_{k=1}^N (\eta_k \epsilon_k + \eta_k u_k^2) + \eta_{He} + \sum_{s=e}^{\alpha} (\eta_s \epsilon_s + \eta_s u_s^2) \right] = 0, \quad (23)$$

$$\frac{d}{d\chi} \left[\eta_H + \sum_{k=1}^N (5\eta_k \epsilon_k u_k + \eta_k u_k^3) + \eta_{He} + \sum_{s=e}^{\alpha} (5\eta_s \epsilon_s u_s + \eta_s u_s^3) \right] = 0, \quad (24)$$

where $\mathcal{R} \equiv \tilde{R}/\bar{R}$.

3.2. Solution Method

Eqs. (15)–(24) are a set of ten coupled, non-linear ordinary differential equations, which are solved with the constraint of charge conservation. We compute eqs. (15)–(22) directly in terms of the number density flux, denoted $y \equiv \eta u$. The ion velocity and temperature, u_i and ϵ_i , determine the broad velocity u_k and temperature ϵ_k through the relations (2)–(3). Once y and u are known, the dimensionless number density $\eta = y/u$ can be substituted into the right hand side of the conservation equations.

We solve eqs. (23) and (24) subject to the boundary conditions $y_H(0) = 1 - f_p$, $y_{He}(0) = (1 - f_p)f_{He}$, $y_p(0) = f_p$, and $y_k(0) = y_{He+}(0) = y_\alpha(0) = 0$. The upstream neutral temperature is taken to be zero, while the protons and electrons are in thermal distributions with $T_u \ll T_p$. Integrating these equations, substituting the initial conditions, and using the definition for y yields:

$$\left(\sum_{k=1}^N F_{v,k} y_k + \sum_{s=p}^{\alpha} y_s \right) u_i^2 + [y_H + y_{He} - 1 - (1 + \beta) f_p \epsilon_u - f_{He}(1 - f_p)] u_i + \left(\sum_{k=1}^N \frac{F_{T,k}}{F_{v,k}} y_k + \beta y_e + \sum_{s=p}^{\alpha} y_s \right) \epsilon_i = 0, \quad (25)$$

$$\left(\sum_{k=1}^N F_{v,k}^2 y_k + \sum_{s=p}^{\alpha} y_s \right) u_i^2 + \left(5 \sum_{k=1}^N F_{T,k} y_k + 5\beta y_e + 5 \sum_{s=p}^{\alpha} y_s \right) \epsilon_i + y_H + y_{He} - 1 - 5(1 + \beta) f_p \epsilon_u - f_{He}(1 - f_p) = 0. \quad (26)$$

Note that the sums over charged species run from protons to alpha particles and do not include electrons, which appear separately in the equations. The system (25)–(26) can be solved simultaneously to yield a quadratic equation in u_i with coefficients that are functions of χ . The solution to the quadratic has two positive roots. Only one of the roots is less than unity; it represents the physical solution for the bulk ion velocity, which must be less than the shock velocity. We use a standard Runge-Kutta method to solve eqs. (15)–(24), at each integration step solving (25)–(26) for the ion velocity which determines the particle densities.

Figure 2 shows the density structure of the shock transition zone for $v_s = 1000 \text{ km s}^{-1}$, $f_p = 0.5$, and $\beta = 1$. Using eq. (14), the spatial coordinate has been converted from χ to physical distance z behind the shock front. We use external density $n_0 = 1 \text{ cm}^{-3}$, distance $d = 1 \text{ kpc}$, and helium fraction $f_{He} = 0.1$ for all calculations in this paper. The left and right panels of Figure 2 show the dimensionless densities for the neutral and charged species, respectively. The electron and proton densities have been scaled by a factor of 1/18.

In the left panel, the solid curve shows a monotonic decrease in density of cold hydrogen atoms, which are removed by both charge transfer and ionization reactions. Charge transfer produces three populations of broad neutrals. At low velocities, charge transfer dominates over ionization, and many broad neutrals with $k > 3$ are produced. The dash-dotted curve shows the density of neutral helium, which is ionized farther downstream than hydrogen due to its smaller ionization rate coefficients. In the right panel, the solid curve shows singly-ionized helium, which is produced downstream from neutral atoms, and is then ionized to produce a monotonically increasing population of alpha particles, shown by the dotted curve. The proton and electron densities are depicted by the short-dashed and long-dashed curves, which saturate when all of the neutral species have been depleted. The final electron density is slightly higher than that of the protons due to the presence of alpha particles.

4. Line Emission

Once the density structure of the transition zone is determined, we can compute the hydrogen line emission, including the spatial distribution and line profiles for the broad and narrow components. We neglect collisional deexcitation and assume that every atom is excited from the ground state. $H\alpha$ photons are produced by transitions from atomic levels $3s$ and $3d$ to $2p$, as well as from $3p$ to $2s$. In the latter case, the atomic physics is complicated by a possible transition from $3p$ directly to $1s$, which results in a Lyman β photon. As discussed by Heng & Sunyaev (2008), if the medium is optically thin to Ly β photons (Case A conditions), the contributions from the angular momentum states can be weighted according to $nl = 3s + 3d + B_{3p,2s}3p$, where the factor $B_{3p,2s} \approx 0.12$ is the fraction of transitions from $3p$ to $2s$. If the medium is optically thick to Ly β photons (Case B conditions), re-absorption by ground state hydrogen effectively traps Ly β emission until the atom produces an $H\alpha$ photon. In this case, all of the transitions eventually result in $H\alpha$ emission, and we set $B_{3p,2s} \approx 1$.

Case A and B conditions represent the two extremes of media that are optically thin and thick to Ly β scattering. We estimate this optical depth for the stationary atoms (i.e., cold hydrogen) which produce the narrow line. At line center, $\tau_\beta \sim n_H \sigma l_{\text{zone}} \gtrsim 10$ for $n_H \sim 1 \text{ cm}^{-3}$, $\sigma \sim 10^{-14} \text{ cm}^2$, with $l_{\text{zone}} \sim 10^{15} \text{ cm}$ (see, e.g., Rybicki & Lightman 1979; Cox 2001). For an optically thick medium, an average Ly β photon will undergo τ_β^2 scatterings (Rybicki & Lightman 1979). At each scattering, there is an 88% chance that the absorbed photon is re-emitted as Ly β ; we estimate that more than 99% of the Ly β emission will be converted to $H\alpha$. Moreover, the column density of cold hydrogen extends beyond the transition zone into the pre-shock ISM, increasing the effective value of τ_β . Therefore, we

expect the narrow emission in the majority of Balmer-dominated SNRs to be described by Case B conditions. In contrast, broad neutrals absorb $\text{Ly}\beta$ too far from line center to scatter many photons, and are always described by Case A conditions.

In the unlikely case that $\tau_\beta \sim 1$, partial scattering of Lyman photons will occur and produce results intermediate between Cases A and B for the narrow line (Ghavamian et al. 2001). We will address this issue in future work.

4.1. Spatial Emissivity Profile

To determine the emission, we use excitation rate coefficients calculated as described by Paper 1 (see also Appendix A). An emission line photon is produced when a cold hydrogen atom or broad neutral is excited by a charged particle, or undergoes charge transfer to an excited state. In the former cases, the rates must be weighted by the probability of repeated excitation. We use the following equations to calculate the spatial emissivity profile for the narrow (ξ_n) and broad (ξ_b) components:

$$\xi_n(z) = \frac{n_H}{1 - P_{E_0}} \sum_{s=e}^{\alpha} n_s \tilde{R}_{\Delta n, E_0, s}, \quad (27)$$

$$\xi_b(z) = n_H n_p \tilde{R}_{\Delta n, T_0^*, p} + \sum_{k=1}^N n_k \left(n_p \tilde{R}_{\Delta n, T^*, p} + \frac{1}{1 - P_E} \sum_{s=e}^{\alpha} n_s \tilde{R}_{\Delta n, E, s} \right), \quad (28)$$

where the rate coefficients are labeled by the transition $\Delta n = H\alpha, \text{Ly}\alpha, \text{Ly}\beta$, particle type, and atomic interaction. The symbols E_0 and T_0^* denote excitation and charge transfer to an excited state for cold hydrogen, while E and T^* denote these interactions for broad neutrals. The probabilities $P_{E_0} = R_{E_0}/(R_{E_0} + R_{I_0} + R_{T_0})$ and $P_E = R_E/(R_E + R_I + R_T)$ are calculated using the total reaction rates per atom or broad neutral for ionization, excitation, and charge transfer. These are calculated using the weighted sum of the rate coefficients, for example, $R_I = \sum_{k=1}^N n_k \sum_{s=e}^{\alpha} n_s \tilde{R}_{iB, s}$.

Figure 3 shows the spatial emissivity profiles for the narrow and broad components as a function of distance z behind the shock front. The thin vertical lines indicate the centroids $z_{cn, b}$ of the emission components, calculated according to the formula:

$$\int_0^{z_{cn, b}} dz \xi_{n, b}(z) - \int_{z_{cn, b}}^{\infty} dz \xi_{n, b}(z) = 0. \quad (29)$$

For the low value of f_p shown in this figure, significant ionization must occur before there are enough charged particles to excite the narrow emission and engage in charge transfers to

produce the broad neutrals. Therefore, the intensity peaks for both components are shifted downstream from the shock front. Moreover, the centroid of the broad line emission is shifted downstream from that of the narrow line.

4.2. Line Profiles

The full width half maximum (FWHM) of the broad line can be related to the velocity and temperature equilibration of the shock. In previous works, the broad line profile was taken to be equal to the projected broad neutral distribution function (e.g., Chevalier et al. 1980; Heng & McCray 2007). The actual line profile must be a convolution of the broad neutral and exciting species distribution functions with the cross sections for excitation and charge transfer to an excited state. In a cylindrical coordinate system (r, θ, z) where the z axis is along the shock velocity direction, it is straightforward to project the line profile for observers oriented both edge-wise (along the r axis) and face-on (along the z axis) with respect to the shock front. Due to limb brightening, most observations will be selected for shocks viewed edge-wise or nearly so.

We calculate hydrogen line profiles ϕ_{FO} , and ϕ_{EW} according to the formulas:

$$\phi_{FO}(v_z) = n_H n_p F_{Tp,z}(v_s) + \int d^3 \mathbf{v}' \left\{ \sum_{k=1}^N n_k f_k(\mathbf{v}') \left[\sum_{s=e}^{\alpha} n_s F_{Es,z}(\mathbf{v}') + n_p F_{Tp,z}(\mathbf{v}') \right] \right\}, \quad (30)$$

$$\phi_{EW}(v_r, z) = n_H n_p F_{Tp,r}(v_s) + \int d^3 \mathbf{v}' \left\{ \sum_{k=1}^N n_k f_k(\mathbf{v}') \left[\sum_{s=e}^{\alpha} n_s F_{Es,r}(\mathbf{v}') + n_p F_{Tp,r}(\mathbf{v}') \right] \right\}, \quad (31)$$

$$F_{Xs,z} = \int_0^{2\pi} d\theta \int_0^{\infty} dv_r v_r f_s(\mathbf{v}) \Delta v [\sigma_{X,3s,s}(\Delta v) + \sigma_{X,3d,s}(\Delta v) + B_{3p,2s} \sigma_{X,3p,s}(\Delta v)], \quad (32)$$

$$F_{Xs,r} = v_r \int_0^{2\pi} d\theta \int_{-\infty}^{\infty} dv_z f_s(\mathbf{v}) \Delta v [\sigma_{X,3s,s}(\Delta v) + \sigma_{X,3d,s}(\Delta v) + B_{3p,2s} \sigma_{X,3p,s}(\Delta v)], \quad (33)$$

where $\Delta \mathbf{v} \equiv |\mathbf{v} - \mathbf{v}'|$, and the cross sections σ denote excitation and charge transfer reactions of atoms to the angular momentum states $3s$, $3p$, and $3d$, for each of the charged particle species. The edge-wise profile can be calculated as a function of position behind the shock. In practice, however, the observed line profiles are not spatially resolved. We therefore calculate the profiles as a function of v_s and β , spatially averaged over the shock transition zone. Figure 4 shows (symmetric) edge-wise velocity line profiles for the broad component of the $H\alpha$ emission, in a reference frame where the average proton velocity is zero. Results are depicted for $\beta = 0.01, 0.1, 0.5, 1$, with $v_s = 1000 \text{ km s}^{-1}$ (left panel), and 8800 km s^{-1} (right panel). For all cases, the pre-shock ionization fraction is set to $f_p = 0.5$.

Figure 5 displays the FWHM of the broad line velocity profile, as a function of v_s , for $H\alpha$ at several values of $\beta = 0.01, 0.1, 0.5, 1$ (left panel), and $H\alpha$, $Ly\alpha$, and $Ly\beta$ at $\beta = 0.1$ (right panel). The FWHM increases monotonically with v_s due to the increased temperature of the broad neutral and ion distributions behind faster moving shocks. As β is increased, energy is transferred from the protons to heat the electrons, leading to lower proton temperatures and a smaller FWHM.

An important consequence of the use of eqs. (30) and (31) to calculate line profiles is that we expect different transitions (e.g., $H\alpha$ and $Ly\alpha$) to have different FWHM relations, since they employ distinct reaction cross sections in the calculation of ϕ (see Figure 5). This is a unique prediction made by our calculation, and may have consequences for studies of $Ly\alpha$ emission from fast shocks ($v_s \gtrsim 4000 \text{ km s}^{-1}$).

5. Dependence on Shock Parameters

Here we describe how the structure and emission from the transition zone of Balmer-dominated shocks depend on shock velocities (ranging from $v_s = 300 - 10,000 \text{ km s}^{-1}$), pre-shock ionization fractions (ranging from $f_p = 0.1 - 0.9$), and temperature equilibration ratios (ranging from $\beta = 0.1 - 1$), as well as Case A and Case B conditions for the narrow line.

5.1. Spatial Structure of the Shock Transition Zone

The basic features of the shock transition zone density structure were shown in Figure 2. The details of broad neutral production are highly sensitive to v_s , f_p , and β . We can see the effect of increasing shock velocity by comparing Figure 6 to Figure 2. At high v_s , the ionization rate is greater than the charge transfer rate, so that relatively few broad neutrals are produced. The densities of the broad neutral populations decrease rapidly with each subsequent charge transfer reaction. The helium ionization rates decrease, causing the He^+ and alpha particle production to peak further downstream.

In Paper 2, we explored variations in ion velocity throughout the shock transition zone and found that, for $v_s \gtrsim 300 \text{ km/s}$, $v_i \approx v_s/4$ with negligible deviation. We confirm this conclusion with our multi-component models. Figure 7 shows the dimensionless ion velocity and temperature as a function of distance from the shock front. Results are shown for $v_s = 1000$ and $v_s = 4000 \text{ km s}^{-1}$, with $f_p = 0.5$, $\beta = 1$. In the left panel, we show the percent deviation of ion velocity from $v_s/4$ for the two shock velocities. At $v_s < 1600$

km s^{-1} , broad neutrals are produced with smaller momentum density than the original ion population, leading to an increase in ion velocity by conservation of momentum (solid curve). For $v_s \gtrsim 1600 \text{ km s}^{-1}$, the opposite occurs, and the ion velocity decreases as the broads are produced (dotted curve). The deviation of ion velocity from $v_s/4$ is less than 1% and has a negligible effect on the hydrodynamics. In the right panel, we plot the ion temperature profile. In this case, the broad neutrals are produced with slightly lower temperature than the ions, leading to slight heating of the ions. At large distance downstream, some of the energy in the ions is transferred to heat the alpha particle population, causing the ion temperature to decrease below the value $3/16(1 + \beta)$. The maximum deviation of ϵ_i from its expected value is of order 10%, which in practice has a negligible effect on the values of the reaction rate coefficients.

5.2. $\text{H}\alpha$ Emissivity

In Figure 3, we showed a typical emissivity profile at relatively low shock velocity and ionization fraction. In the left panel of Figure 8, we show the effect of increasing the initial ionization fraction to $f_p = 0.9$. We see that the neutral density decreases rapidly and the narrow line emission peaks at the shock front (left panel). Many charge transfer reactions occur close to the shock, pushing the centroid of the broad emission further upstream compared to the $f_p = 0.1$ case. Comparing the right panel of Figure 8 to Figure 3, we can see the effect of increasing the shock velocity. For the high velocity case, both ionization and charge transfer rates are decreased, shifting the centroids of both line components further downstream in the transition zone.

As discussed in Raymond et al. (2007) and Paper 2, the spatial shift between the broad and narrow line centroids potentially provides an important constraint on the pre-shock ionization fraction, f_p , and external density, n_0 . In Figure 9, we plot $z_{\text{sh}} = z_{cb} - z_{cn}$ as a function of shock velocity v_s . In the left panel, we show how these results depend on f_p , holding $\beta = 1$. As the velocity increases, the charge transfer rate decreases relative to the ionization rate, delaying the production of broad neutrals. Consequently, the centroid of ξ_b shifts downstream and the value of z_{sh} increases. For small f_p , few protons initially exist to engage in charge exchange. Consequently, z_{cb} shifts downstream from the shock front. In the right panel, we show how the results depend on the temperature equilibration parameter, β , for fixed $f_p = 0.5$. At low velocities, increasing β tends to cause the proton ionization rate for broad neutrals to dominate over that for cold hydrogen. This effect causes the peak of broad production to shift downstream from shock front. At high velocities, increasing β tends to increase the charge transfer rate for broad neutrals over that for cold hydrogen. This effect

causes the peak of broad production to shift closer to the shock front, and decreases the value of z_{sh} . For more discussion on the observational significance of the spatial emissivity profile and the shift, see §6.3.

Another important observational diagnostic for Balmer-dominated SNRs is the ratio of broad-to-narrow integrated line strengths, defined as:

$$I_b/I_n = \frac{\int_0^\infty dz \xi_b(z)}{\int_0^\infty dz \xi_n(z)}. \quad (34)$$

This ratio has a strong dependence on both v_s and β . Figure 10 shows I_b/I_n versus shock velocity at fixed $f_p = 0.5$, for several values of temperature equilibration $\beta = 0.1, 0.5, 1$, using Case A (left panel) and Case B (right panel) conditions for the narrow line. For a given β , the variation of the intensity ratio with velocity is the result of a competition between charge transfer and ionization rates, which are roughly equal at $v_s \sim 2000 \text{ km s}^{-1}$. At very low v_s , the ionization rate begins to decrease precipitously while the charge transfer rate stays roughly constant, leading to the spike in I_b/I_n . At a fixed shock velocity, increasing β causes a decrease in the proton ionization rate for broad neutrals compared to cold hydrogen, leading to an increase in the intensity ratio. In Case B conditions (right), additional narrow emission due to absorption of trapped Ly β photons decreases the values of I_b/I_n relative to Case A (see the discussion in §2).

Previous models have given conflicting results for the dependence of I_b/I_n on f_p (e.g., Ghavamian et al. 2001; Heng & McCray 2007; Heng et al. 2007). According to the picture in Paper 1, we expect any such dependence to be weak, since the number of broad neutrals produced in each population per cold hydrogen atom is fixed. This intuition is confirmed by our multi-component calculation. When f_p is increased, we expect more charge transfers in the shock transition zone. However, this effect is balanced by higher ionization rates of both the broad neutral and narrow populations from which the broad neutrals are produced. The net result is a negligible change in the I_b/I_n ratio. The presence of neutral helium introduces a weak dependence of I_b/I_n on f_p . In Figure 11, we show I_b/I_n as a function of v_s for fixed $\beta = 1$ in Case A (left panel) and Case B (right panel) conditions. As f_p increases, more protons engage in charge transfer and ionization reactions close to the shock front, shifting the peak of broad neutral production upstream. In this case, the broad neutrals do not persist far enough downstream to interact with the charged helium species produced there, altering the ratio I_b/I_n . Note that this effect is of order $\lesssim 1\%$ for $f_{\text{He}} = 0.1$ and remains small for larger helium fractions. Thus, the broad-to-narrow intensity ratio can be written as a function

$$I_b/I_n = L_{bn}(v_s, \beta), \quad (35)$$

where I_b/I_n and L_{bn} represent the measured and theoretical values of the intensity ratio, respectively. The insensitivity of this ratio to f_p is critical for accurately inferring v_s and β from observations.

5.3. Broad Line Profiles and Observational Interpretations

Eqs. (30) and (31) allow us to model the FWHM of the broad line as a function of v_s and β , as shown in Figs. 4–5. Note that the FWHM has a weak ($\lesssim 1\%$) dependence on the pre-shock ionization after taking a spatial average over the shock transition zone. Figure 12 shows broad line velocity profiles for the case of face-on orientation of the shock as a function of line-of-sight velocity v_r , in a frame of reference where the proton velocity is zero. Results are shown for fixed $f_p = 0.5$ at several values of $\beta = 0.01, 0.1, 0.5, 1$ at shock velocities $v_s = 1000 \text{ km s}^{-1}$ (left panel) and $v_s = 8800 \text{ km s}^{-1}$ (right panel). At low shock velocities, charge transfer is extremely efficient, yielding broad neutral distribution functions nearly identical to that of the thermal protons. At high shock velocities, the broad neutral distributions are skewed and offset from the proton distribution, leading to the asymmetric line profiles depicted in the right panel.

Figure 5 demonstrates that the FWHM relation can be written as a function (ignoring the unimportant dependence on f_p) of v_s and β :

$$W_{\text{FWHM}} = W(v_s, \beta), \quad (36)$$

where W_{FWHM} and W represent the measured and theoretical values of the line FWHM, respectively. For SNRs with measured W_{FWHM} and I_b/I_n , combining eqs. (35) and (36) self-consistently constrains v_s and β . To accomplish this, one inverts $W(v_s, \beta)$ to yield $v_s = W^{-1}(W_{\text{FWHM}}, \beta)$, and calculates the root of the expression

$$L_{bn} [W^{-1}(W_{\text{FWHM}}, \beta), \beta] - I_b/I_n = 0. \quad (37)$$

This procedure produces a pair of values (v_s, β) for which the theoretical calculations L_{bn} and W equal the measured I_b/I_n and W_{FWHM} .

We emphasize that a self-consistent calculation is critical for accurately determining the values of v_s and β . In the previous literature, it has been common practice to choose two bracketing values for the temperature equilibration (e.g., $\beta = 0.1, 1$) and then to employ the FWHM relation to give a range of possible values for the shock velocity (e.g., Ghavamian et al. 2001; Heng & McCray 2007). However, this procedure has a major flaw. In practice, the self-consistent quantity $L_{bn} [W^{-1}(W_{\text{FWHM}}, \beta), \beta]$ will have a minimum value

over the range $\beta \in (m_e/m_p, 1)$. If I_b/I_n for a particular observed shock is less than this minimum value, then no pair of values (v_s, β) will yield the observed values I_b/I_n and W_{FWHM} . In such a case, the model breaks down and quoting a range of possible shock velocities for two bracketing values of β is inappropriate. An additional mechanism must be invoked to account for the observations. Moreover, when no measurement of I_b/I_n exists, the bracketing procedure may or may not yield an accurate estimate of the range of shock velocities.

We use the methodology described above to self-consistently extract shock parameters from observations of Balmer-dominated SNRs. We summarize our results in Table 1, which lists, from left to right, the object, reference, $\text{H}\alpha$ W_{FWHM} and I_b/I_n , calculated values for v_s and β from $\text{H}\alpha$, $\text{Ly}\beta$ W_{FWHM} , and calculated value for v_s from $\text{Ly}\beta$. If our models do not yield a fit to the observations, we do not list values for the shock velocity and temperature equilibration ratio. Our calculations show a characteristic range of β between 0.01 and 0.1. Therefore, in the case of $\text{Ly}\beta$ observations where no measurement of I_b/I_n exists, we report derived shock velocities for the range $\beta = 0.01 - 0.1$; further observations are required to confirm the accuracy of these estimates. For SNR 0519-69.0, observations exist in $\text{H}\alpha$ and $\text{Ly}\beta$. To calculate shock velocities from the $\text{Ly}\beta$ observations, we use the derived value of β from the $\text{H}\alpha$ diagnostics. The estimates from both bands agree with each other within the observational uncertainty. The object DEM L71/0505-67.9 shows anomalous behavior and likely requires additional physics to properly model (see §6.3). If we exclude this object from our considerations, we can successfully fit 12 out of 14 measurements from seven SNRs within the observational uncertainties. In the cases of the Cygnus Loop (Ghavamian et al. 2001), and an early measurement of 0519-69.0 (Smith et al. 1991), the observed ratio I_b/I_n is too low to be accounted for by our calculations. We discuss probable explanations for these discrepancies below.

We note that our inferred shock velocities and temperature equilibration ratios are systematically lower than in previous studies, including Ghavamian et al. (2001), and Papers 1 and 2. Typically, inferred values for v_s are $\sim 30 - 50\%$ smaller than those quoted in Paper 1. The reason for this discrepancy is that previous work underestimated the effect of broad neutrals in the shock transition zone and used a projected broad neutral velocity distribution rather than the full line profile to determine the broad FWHM.² Thus, these models have consistently smaller predicted values for L_{bn} and W than those presented in this paper. In addition, our models show an increased sensitivity to β compared to Papers 1 and 2. This is due to the factors of density which appear in the calculations of intensity ratio and FWHM, and the dependence of the reaction rate coefficients on the details of the thermal proton and

²In addition, previous calculations did not properly take into account the distribution of atomic transitions between distinct angular momentum states.

electron distributions. The ability to sensitively probe both shock velocity and temperature equilibration is of interest for studies of collisionless electron heating in shocks, as described below.

6. Discussion

6.1. Collisionless Shock Heating

One of the motivations for studying Balmer-dominated SNRs is to probe the physics of collisionless shocks. While various mechanisms for transferring energy from proton to electron populations have been proposed in the literature, there is no consensus on how to predict the value of β for a given set of shock parameters in astrophysical contexts. In a recent paper, Ghavamian et al. (2007b) attempted to address this problem by deriving a relation for temperature equilibration ratio versus shock velocity from observations of shocks in SNRs. They reported that their results could be fit by a curve $\beta(v_s) \propto v_s^{-2}$, with $\beta = 1$ for $v_s \leq 400 \text{ km s}^{-1}$. Given that the proton temperature scales roughly as $T_p \propto v_s^2$, this conclusion implies that the electrons are heated to a constant temperature, independently of the shock velocity. While Ghavamian et al. (2007b) discussed a possible mechanism for this dependence, it has not been established that theoretical models can produce such an effect.

Using our new model for emission from Balmer-dominated shocks, we have calculated an updated $\beta(v_s)$ relation, which is displayed in Figure 13. For all the points shown in the plot, we have self-consistently fit measurements of both W_{FWHM} and I_b/I_n . The derived v_s and β are insensitive to the assumed value of the pre-shock ionization, which we take to be $f_p = 0.1$. If we exclude the calculations associated with SNR 0505-67.9, we are able to fit these points to a power-law curve, obtaining $\beta(v_s) \propto v_s^{-\alpha}$, with $\alpha = 1.23 \pm 0.04$ and reduced chi-square $\chi_r^2 = 16/10 = 1.6$.³ The fit is shown by the bottom curve in Figure 13, while the v_s^{-2} dependence from Ghavamian et al. (2007b) is shown by the top curve.

Our new results contrast sharply with those of previous models. It is clear from Figure 13 that, even with the SNR 0505-67.9 points left in, $\beta(v_s)$ is not consistent with an inverse-squared power-law. Moreover, while the data roughly match a power-law with flatter index, they might also be regarded as clustered into two distinct regimes at low and high velocities. Further observations of shocks with velocities $v_s \sim 500 - 1000 \text{ km s}^{-1}$ and $W_{\text{FWHM}} \sim 800 - 1500 \text{ km s}^{-1}$ are required to fully delineate the $\beta(v_s)$ curve. In any case, we conclude

³For $f_p = 0.9$, the values become $\alpha = 1.19 \pm 0.05$, with $\chi_r^2 = 1.8$. If we force $\alpha = 2$ in our fit, we find an unacceptable $\chi_r^2 \approx 25$.

that electron populations in fact achieve higher temperatures at greater shock velocities. The minimum value of the temperature equilibration ratio is $\beta \sim 0.03$ at velocities $v_s \gtrsim 1500 \text{ km s}^{-1}$. This value is greater by several orders of magnitude than the theoretical minimum $\beta = m_e/m_p$, but is significantly smaller than the value predicted by collisionless heating models (e.g., Cargill & Papadopoulos 1988; Rakowski et al. 2003).

There are several reasons for the differences between our results and those of Ghavamian et al. (2007b). As discussed above, our new models systematically infer lower values for v_s and β , leading to a smaller α for the putative $\beta(v_s)$ curve. In addition, Ghavamian et al. (2007b) constructed their curve using 11 total points, 5 of which were taken from SNR 0505-67.9. Ghavamian et al. (2003) made a total of 14 measurements of 0505-67.9, most of which cannot be fit by current or previous models. It is therefore unclear why only 5 were used to construct their β curve. In general, SNR 0505-67.9 displays some anomalous properties, which call into question its interpretation according to the standard Balmer-shock model. As shown in Ghavamian et al. (2003), the narrow component for this object has widths of order $W_{\text{FWHM}} \gtrsim 100 - 200 \text{ km s}^{-1}$, which are more than an order of magnitude higher than those observed in other remnants. As a result, the observed I_b/I_n ratios are much lower than those predicted by our current or previous models and we can self-consistently fit only three of the measurements from SNR 0505-67.9, obtaining values inconsistent with those of other SNRs (see Figure 13). It is likely that additional physics (e.g., a cosmic-ray precursor or clumpy circumstellar medium) are required to model the emission from this object. Indeed, Ghavamian et al. (2007b) remark that for one of their points, they are unable to fit both the FWHM and intensity ratio. In this case, they are forced to use the broad component FWHM alone to constrain the shock velocity and proton temperature, and infer the electron temperature from *Chandra Observatory* X-ray spectra (Rakowski et al. 2003; Rakowski 2005). As argued above, using only the FWHM to infer v_s is not appropriate. Furthermore, it is not obvious that the electron temperature derived from X-rays will be the same as that in the shock transition zone. At this point, the data from SNR 0505-67.9 are difficult to interpret and additional work is required to draw conclusions about collisionless shock heating from them. In addition, another of the data points used by Ghavamian et al. (2007b), for the Cygnus loop, likely is described by a partially radiative shock model, as discussed below.

6.2. Limitations to our Model

In addition to SNR 0505-67.9, our calculations cannot account for the low observed values for I_b/I_n from the Cygnus Loop and one data point of SNR 0519-69.0 (see Table 1). The Cygnus Loop has the lowest measured FWHM in our sample, and, given its age of

$\sim 20,000$ years, likely has a shock velocity $v_s \lesssim 100 \text{ km s}^{-1}$. At such low values of v_s , our shock emission model breaks down, as radiative contributions from metal transitions become important (e.g, Shull & McKee 1979). Portions of the Cyngus Loop have likely made transitions from non-radiative to partially radiative shock conditions (Hester et al. 1994). Thus, it is not surprising that we are unable to properly model the Cyngus Loop.

In the case of 0519-69.0, earlier observations by Tuohy et al. (1982) resulted in higher measured broad line widths. These observations are well fit by our calculations. However, the $\text{H}\alpha$ flux from the later Smith et al. (1991) measurement is dominated by emission from a bright knot on the eastern rim of the remnant, likely a high-density region with lower shock velocity (see §3.3 of Ghavamian et al. 2007a).

In §4 we argued that the narrow emission from most Balmer-dominated SNRs should be described by Case B conditions. We did not attempt to calculate the effects of partial $\text{Ly}\beta$ scattering in the shock transition zone. Note that the low observed values of I_b/I_n confirm our expectations based on physical arguments, as Case A or partial scattering conditions will lead to theoretical values for I_b/I_n which are too high for most Balmer-dominated SNRs (see Figure 10). Nevertheless, Lyman scattering in a shock transition zone may have interesting applications for other classes of objects which we discuss below.

6.3. Future Work

As demonstrated by SNR 0505-67.9, some additional physical mechanism is needed to account for the observed $\text{H}\alpha$ emission seen in some SNRs. One possibility is that a significant amount of the dissipated energy in the shock is transferred to cosmic-rays, producing a precursor which can heat and accelerate the upstream gas and alter the shock jump conditions and downstream proton and electron populations (Blandford & Eichler 1987; Drury et al. 2001). These effects will change the structure of the transition zone and the kinetic rates calculated from the charged species distribution functions. In addition, the precursor can “push” on the upstream protons, leading to a velocity differential between neutrals and charged species (e.g., Berezhko & Ellison 1999). The resulting upstream atomic interactions, may further broaden the narrow component of the $\text{H}\alpha$ line. Evidence exists for such precursors in the anomalously large widths of $\text{H}\alpha$ lines in some Balmer-dominated SNRs (e.g., observations of DEM L71/0505-67.9 by Ghavamian et al. 2003).

Another possible way to account for the large narrow component widths is to assume that the shock propagates into a clumpy circumstellar medium. In this case, the shock can “wrap around” density inhomogeneities. Instead of observing an edge-wise shock, emission

comes from several orientations relative to the observer resulting in a broadened narrow $H\alpha$ line component.

The spatial structure of the shock transition zone provides a possible way to infer the external density n_0 and pre-shock ionization fraction f_p . As noted in §5.2 the spatial emissivity profile and centroid shift between the narrow and broad components have a strong dependence on f_p and n_0 . Raymond et al. (2007) were able to spatially resolve the total $H\alpha$ emission from SN1006 using the ACS camera on the *Hubble Space Telescope*. Using earlier model calculations for the broad neutral interactions and transition zone structure, Raymond et al. (2007) inferred v_s and β from the FWHM and I_b/I_n , and then attempted to fit for the spatial structure by varying f_p and n_0 . Future instruments similar to ACS with high spatial resolution (e.g., WFC3 onboard *Hubble* with the narrow $H\alpha$ component isolated by a narrow band filter) will allow for more accurate measurements of the transition zone structure and provide additional constraints on shock parameters.

The models presented in our series of papers generically describe the physics of non-radiative shocks interacting with cold, pre-shock gas and may be applied to both collisional and collisionless shocks. Besides using them to understand nearby SNRs, we can also model hydrogen line emission from SNRs in young, distant galaxies (with $z \sim 3 - 5$), a subject first explored by Heng & Sunyaev (2008). We improve on their estimates of the luminosity ratios of $Ly\alpha$ and $Ly\beta$ to $H\alpha$, denoted $\Gamma_{Ly\alpha/H\alpha}$ and $\Gamma_{Ly\beta/H\alpha}$, respectively (see Figure 14; c.f. Figure 1 of Heng & Sunyaev 2008). Heng & Sunyaev (2008) underestimated the broad $Ly\alpha$ emission at high shock velocities due to their neglect of the multi-component shock transition zone. Nevertheless, their conclusions remain intact: the sensitivity of $\Gamma_{Ly\alpha/H\alpha}$ and $\Gamma_{Ly\beta/H\alpha}$ to β by a factor ~ 2 over the velocity range $1000 \lesssim v_s \lesssim 4000 \text{ km s}^{-1}$ is a direct and unique way to measure the temperature ratio. A valuable extension to their work will incorporate models of $Ly\alpha$ and $Ly\beta$ scattering, taking into account geometric effects.

Our models can also be applied to higher density regimes. For example, broad and narrow $H\alpha$ lines have been observed in “Type Ia/IIn” supernovae (SNe) such as SN 2005gj, which may be thermonuclear SNe exploding into dense ($n_0 \sim 10^7 \text{ cm}^{-3}$) circumstellar hydrogen envelopes. Using a shock model to interpret the broad $H\alpha$ line widths and broad-to-narrow intensity ratios probes the density and velocity structures of the circumstellar material, and explains why the medium has significant optical depth to Balmer lines (Case C conditions, see Xu et al. 1992). Such a study is described in detail by Heng et al. (2008).

We thank Carles Badenes, Anatoly Spitkovsky and Eliot Quataert for useful conversations. K.H. thanks the Institute for Advanced Study for their generous support.

A. Shock Kinetics

We summarize the salient points for our calculations of rate coefficients, broad neutral velocity distributions and broad line profiles. For a more detailed description of our methods, see Paper 1. In this work, we treat the nl atomic sub-levels separately instead of considering a single, summed n level as in Paper 1. We treat charge transfers, excitation and ionization events between electrons, protons, alpha particles and hydrogen atoms using the cross sections of Barnett et al. (1990), Belkić et al. (1992), Janev & Smith (1993), Balança et al. (1998), and Harel et al. (1998). Fitting functions for some of these cross sections are provided in Heng & Sunyaev (2008).

We also consider the ionization of helium atoms and singly-ionized helium by electrons and protons, using the cross sections of Peart et al. (1969), Angel et al. (1978), Rudd et al. (1983), Shah & Gilbody (1985), Rinn et al. (1986) and Shah et al. (1988). Following Heng & Sunyaev (2008), we fit the cross sections to the function

$$\mathcal{F}(x; \mathbf{A}) = \exp \left(\frac{A_0}{2} + \sum_{i=1}^8 A_i \mathcal{C}_i(x) \right), \quad (\text{A1})$$

where the components of $\mathbf{A} = (A_1, A_2, \dots, A_8)$ are the fitting parameters. The quantities \mathcal{C}_i are the Chebyshev orthogonal polynomials:

$$\mathcal{C}_1(x) = x, \quad (\text{A2})$$

$$\mathcal{C}_2(x) = 2x^2 - 1, \quad (\text{A3})$$

$$\mathcal{C}_3(x) = 4x^3 - 3x, \quad (\text{A4})$$

$$\mathcal{C}_4(x) = 8(x^4 - x^2) + 1, \quad (\text{A5})$$

$$\mathcal{C}_5(x) = 16x^5 - 20x^3 + 5x, \quad (\text{A6})$$

$$\mathcal{C}_6(x) = 32x^6 - 48x^4 + 18x^2 - 1, \quad (\text{A7})$$

$$\mathcal{C}_7(x) = 64x^7 - 112x^5 + 56x^3 - 7x, \quad (\text{A8})$$

$$\mathcal{C}_8(x) = 128x^8 - 256x^6 + 160x^4 - 32x^2 + 1. \quad (\text{A9})$$

We define the fitting variable x as

$$x = \frac{\ln(E/E_{\min}) - \ln(E_{\max}/E)}{\ln(E_{\max}/E_{\min})}, \quad (\text{A10})$$

where E is the relative energy between the interacting particles and E_{\min} and E_{\max} are the minimum and maximum energies for which data are available. We assume a fiducial error of 10% for the data. The cross sections and corresponding fits are displayed in Figure 15 and the fitting parameters are presented in Table 2.

We neglect charge transfer reactions of neutral and singly-ionized helium with protons due to scarcity of cross sections for these processes in our velocity range of interest. While such interactions may affect helium line emission, we do not expect them to strongly couple to Balmer radiation. In addition, we approximate excitation and ionization of hydrogen by He^+ using relevant proton rate coefficients due to the lack of appropriate cross sections in the literature.⁴

We make several approximations to speed up our computations. For temperature ratios $0.01 \lesssim \beta \lesssim 0.1$, the velocity width of the electron distribution is generally broader than that of the broad neutrals (characteristic electron velocities are greater than proton velocities by a factor of 4 – 14), implying that rate coefficients for interactions involving electrons are insensitive to changes in the broad neutral velocity distribution. We therefore approximate electron rate coefficients to be the same for reactions involving cold atoms and broad neutrals. Calculations of the FWHM for line profiles should include excitations by electrons, protons, singly-ionized helium and alpha particles. However, alpha particles contribute $\lesssim 1\%$ due to the relatively smaller density n_α . Electron contributions are only important at shock velocities $v_s \lesssim 1000 \text{ km s}^{-1}$, where $\beta \gtrsim 0.1$ and $v_e \gtrsim 14v_p$. In this regime, the line profile contribution due to electrons takes the form of a broad “continuum” relative to the proton contributions. Thus, the line profile widths are predominantly determined by charge transfers and excitations of broad neutrals by protons.

B. Typographical Errors in Papers 1 & 2

We point out several minor typographical errors in Heng & McCray (2007) and Heng et al. (2007). In §5.1 of Heng & McCray (2007), $\mathcal{R}_{bn}(\text{H}\alpha) = I_b(\text{H}\alpha)/I_b(\text{H}\alpha)$ should be $\mathcal{R}_{bn}(\text{H}\alpha) = I_b(\text{H}\alpha)/I_n(\text{H}\alpha)$. In §5 of Heng et al. (2007), $R_{\text{H}\alpha b_0}$ should be $R_{\text{H}\alpha, b_0}$, $R_{\text{H}\alpha b_*}$ should be $R_{\text{H}\alpha, b_*}$ and $R_{\text{H}\alpha n}$ should be $R_{\text{H}\alpha, n}$. In §6.2, paragraph 2, the sentence that begins “Before CKR80 and HM07, ...” should be changed to “Before (CKR80 and HM07), ...”.

⁴Our assumption is based on the Weizsacker-Williams approximation in which scattering dynamics are dominated by the charge of the impacting particle as opposed to its mass (e.g., Jackson 1998). This approximation is valid when the relative velocity of the collision is greater than that of an electron orbiting the hydrogen atom. At low velocities $v_s \gtrsim 300 \text{ km s}^{-1}$, this assumption breaks down. Nevertheless, we expect corrections to these cross sections to have a small quantitative effect on our results.

REFERENCES

- Angel, G. C., Dunn, K. F., Sewell, E. C., & Gilbody, H. B. 1978, *Journal of Physics B Atomic Molecular Physics*, 11, L49
- Balança, C., Lin, C. D., & Feautrier, N. 1998, *Journal of Physics B Atomic Molecular Physics*, 31, 2321
- Barnett, C. F., Hunter, H. T., Fitzpatrick, M. I., Alvarez, I., Cisneros, C., & Phaneuf, R. A. 1990, *NASA STI/Recon Technical Report N*, 91, 13238
- Belkić, D., Gayet, R., & Salin, A. 1992, *Atomic Data and Nuclear Data Tables*, 51, 59
- Berezhko, E. G. & Ellison, D. C. 1999, *ApJ*, 526, 385
- Blandford, R. & Eichler, D. 1987, *Phys. Rep.*, 154, 1
- Cargill, P. J. & Papadopoulos, K. 1988, *ApJ*, 329, L29
- Chevalier, R. A., Kirshner, R. P., & Raymond, J. C. 1980, *ApJ*, 235, 186
- Chevalier, R. A. & Raymond, J. C. 1978, *ApJ*, 225, L27
- Cox, A. 2001, *Allen’s Astrophysical Quantities* (Springer Verlag)
- Drury, L. O., Ellison, D. E., Aharonian, F. A., Berezhko, E., Bykov, A., Decourchelle, A., Diehl, R., Meynet, G., Parizot, E., Raymond, J., Reynolds, S., & Spangler, S. 2001, *Space Science Reviews*, 99, 329
- Fesen, R. A., Becker, R. H., Blair, W. P., & Long, K. S. 1989, *ApJ*, 338, L13
- Ghavamian, P., Blair, W. P., Sankrit, R., Raymond, J. C., & Hughes, J. P. 2007a, *ApJ*, 664, 304
- Ghavamian, P., Laming, J. M., & Rakowski, C. E. 2007b, *ApJ*, 654, L69
- Ghavamian, P., Rakowski, C. E., Hughes, J. P., & Williams, T. B. 2003, *ApJ*, 590, 833
- Ghavamian, P., Raymond, J., Smith, R. C., & Hartigan, P. 2001, *ApJ*, 547, 995
- Ghavamian, P., Winkler, P. F., Raymond, J. C., & Long, K. S. 2002, *ApJ*, 572, 888
- Harel, C., Jouin, H., & Pons, B. 1998, *Atomic Data and Nuclear Data Tables*, 68, 279
- Heng, K. & McCray, R. 2007, *ApJ*, 654, 923

- Heng, K. & Sunyaev, R. A. 2008, A & A, in press
- Heng, K., van Adelsberg, M., McCray, R., & Raymond, J. C. 2007, ApJ, 668, 275
- Heng, K., van Adelsberg, M., & Zheng, Z. 2008, ApJ, submitted
- Hester, J. J., Raymond, J. C., & Blair, W. P. 1994, ApJ, 420, 721
- Jackson, J. D. 1998, Classical Electrodynamics, 3rd Edition (New York: Wiley & Sons)
- Janev, R. & Smith, J. 1993, Cross Sections for Collision Processes of Hydrogen Atoms with Electrons, Protons, and Multiply Charged Ions (Vienna: International Atomic Energy Agency)
- Kirshner, R., Winkler, P. F., & Chevalier, R. A. 1987, ApJ, 315, L135
- Mikhailovskii, A. B. 1992, Electromagnetic Instabilities in an Inhomogeneous Plasma (Cambridge: University Press)
- Peart, B., Walton, D. S., & Dolder, K. T. 1969, Journal of Physics B Atomic Molecular Physics, 2, 1347
- Rakowski, C. E. 2005, Advances in Space Research, 35, 1017
- Rakowski, C. E., Ghavamian, P., & Hughes, J. P. 2003, ApJ, 590, 846
- Raymond, J. C., Korreck, K. E., Sedlacek, Q. C., Blair, W. P., Ghavamian, P., & Sankrit, R. 2007, ApJ, 659, 1257
- Rinn, K., Melchert, F., Rink, K., & Salzborn, E. 1986, Journal of Physics B Atomic Molecular Physics, 19, 3717
- Rudd, M. E., Goffe, T. V., Dubois, R. D., Toburen, L. H., & Ratcliffe, C. A. 1983, Phys. Rev. A, 28, 3244
- Rybicki, G. B. & Lightman, A. P. 1979, Radiative Processes in Astrophysics (New York: Wiley-Interscience)
- Shah, M. B., Elliott, D. S., McCallion, P., & Gilbody, H. B. 1988, Journal of Physics B Atomic Molecular Physics, 21, 2751
- Shah, M. B. & Gilbody, H. B. 1985, Journal of Physics B Atomic Molecular Physics, 18, 899
- Shull, J. M. & McKee, C. F. 1979, ApJ, 227, 131

- Smith, R. C., Kirshner, R. P., Blair, W. P., & Winkler, P. F. 1991, *ApJ*, 375, 652
- Spitzer, L. 1962, *Physics of Fully Ionized Gases* (Physics of Fully Ionized Gases, New York: Interscience (2nd edition), 1962)
- Tuohy, I. R., Dopita, M. A., Mathewson, D. S., Long, K. S., & Helfand, D. J. 1982, *ApJ*, 261, 473
- Vink, J., Laming, J. M., Gu, M. F., Rasmussen, A., & Kaastra, J. S. 2003, *ApJ*, 587, L31
- Xu, Y., McCray, R., Oliva, E., & Randich, S. 1992, *ApJ*, 386, 181

Table 1: Inferred Shock Velocities and Temperature Equilibration Ratios from SNRs

Object	Reference	H α FWHM (km s ⁻¹)	H α I_b/I_n	H α v_s (km s ⁻¹)	β	Ly β FWHM (km s ⁻¹)	Ly β v_s (km s ⁻¹)
Cygnus	G01	262 \pm 32	0.59 \pm 0.3	—	—	—	—
RCW 86	G01	325 \pm 10	1.06 \pm 0.1	190 ⁺¹⁶ ₋₁₅	0.359 \pm 0.044	—	—
	G07b	562 \pm 18	1.18 \pm 0.03	366 \pm 15	0.195 ^{+0.013} _{-0.008}	—	—
	G07b	640 \pm 35	1.0 \pm 0.2	431 ⁺⁵³ ₋₃₂	0.197 ^{+0.138} _{-0.038}	—	—
0505—67.9	S91	580 \pm 70	\gtrsim 0.7	—	—	—	—
	G03	785 ⁺⁹⁵ ₋₈₀	0.93 ^{+0.11} _{-0.10}	544 ⁺²³⁶ ₋₆₆	0.192 ^{+0.529} _{-0.046}	—	—
	G03	1055 ⁺¹⁵⁰ ₋₁₂₀	0.88 ^{+0.11} _{-0.10}	919 ⁺¹²⁶ ₋₂₆₄	0.583 ^{+0.081} _{-0.426}	—	—
	G07a	—	—	—	—	1135 \pm 30	737 \pm 22*
	G07a	—	—	—	—	1365 \pm 75	920 ^{+67*} ₋₆₃
0548—70.4	S91	760 \pm 140	1.1 \pm 0.2	513 ⁺¹²⁵ ₋₁₀₆	0.152 ^{+0.103} _{-0.072}	—	—
0519—69.0	S91	1300 \pm 200	0.8 \pm 0.2	—	—	—	—
	T82	2800 \pm 300	0.4—0.8 [‡]	2221 ⁺⁴⁶⁰ ₋₂₈₉	0.039 ^{+0.113} _{-0.012}	—	—
	G07a	—	—	—	—	3130 \pm 155	2495 ⁺³³⁵ ₋₁₅₈
Kepler	F89	1750 \pm 200	1.1 \pm 0.25	1286 ⁺³⁰⁶ ₋₁₆₆	0.025 ^{+0.292†} ₋₀	—	—
Tycho	G01	1765 \pm 110	0.67 \pm 0.1	1303 ⁺⁹⁵ ₋₉₄	0.031 \pm 0.003	—	—
	KWC87	1800 \pm 100	1.08 \pm 0.16	1329 ⁺¹⁸⁰ ₋₈₄	0.025 ^{+0.175} _{-0.001}	—	—
	S91	1900 \pm 300	0.77 \pm 0.09	1417 ⁺²⁶³ ₋₂₅₄	0.031 ^{+0.006} _{-0.004}	—	—
SN 1006	G02	2290 \pm 80	0.84 ^{+0.03} _{-0.01}	1751 ⁺⁶⁹ ₋₇₀	0.030 ^{+0.001} _{-0.003}	—	—
	S91	2310 \pm 210	0.73 \pm 0.06	1773 ⁺¹⁸⁷ ₋₁₈₄	0.035 ^{+0.003} _{-0.007}	—	—
	KWC87	2600 \pm 100	0.77 \pm 0.08	2021 ⁺¹⁵⁶ ₋₉₃	0.027 ^{+0.053} _{-0.005}	—	—
0509—67.5	G07a	—	—	—	—	3710 \pm 400	3085 ^{+561*} ₋₄₅₄

Note: Results are shown for Case B conditions, and are insensitive to the pre-shock ionization fraction, taken to be $f_p = 0.1$. For full references, see §1.

*: Values are reported for the range $0.01 \leq \beta \leq 0.1$.

†: We exclude values in the H α FWHM and I_b/I_n ranges that are inconsistent with our models.

‡: We regard this as 0.6 ± 0.2 when constructing our $\beta(v_s)$ curve.

Table 2: Fits to Helium Species Ionization Cross Sections

	He + e ⁻	He ⁺ + e ⁻	He + p	He ⁺ + p
A_0	-78.4712	-82.6155	-77.0261	-80.7740
A_1	-0.832236	-0.535745	0.596233	1.50686
A_2	-1.00452	-1.15893	-1.37165	-2.04982
A_3	0.482606	0.644513	0.205854	0.384422
A_4	-0.244927	-0.419765	0.123038	0.353731
A_5	0.121965	0.299795	-0.0671246	-0.268015
A_6	-0.0795100	-0.204216	-0.0135306	-0.0107265
A_7	0.0537985	0.133238	0.0163305	0.0101069
A_8	-0.0521662	-0.0716388	-0.00556328	-0.110770
E_{\min}	26.6 eV	54.5 eV	5.0 keV	2.98 keV
E_{\max}	10^4 eV	10^4 eV	2.38×10^3 keV	1.03×10^3 keV

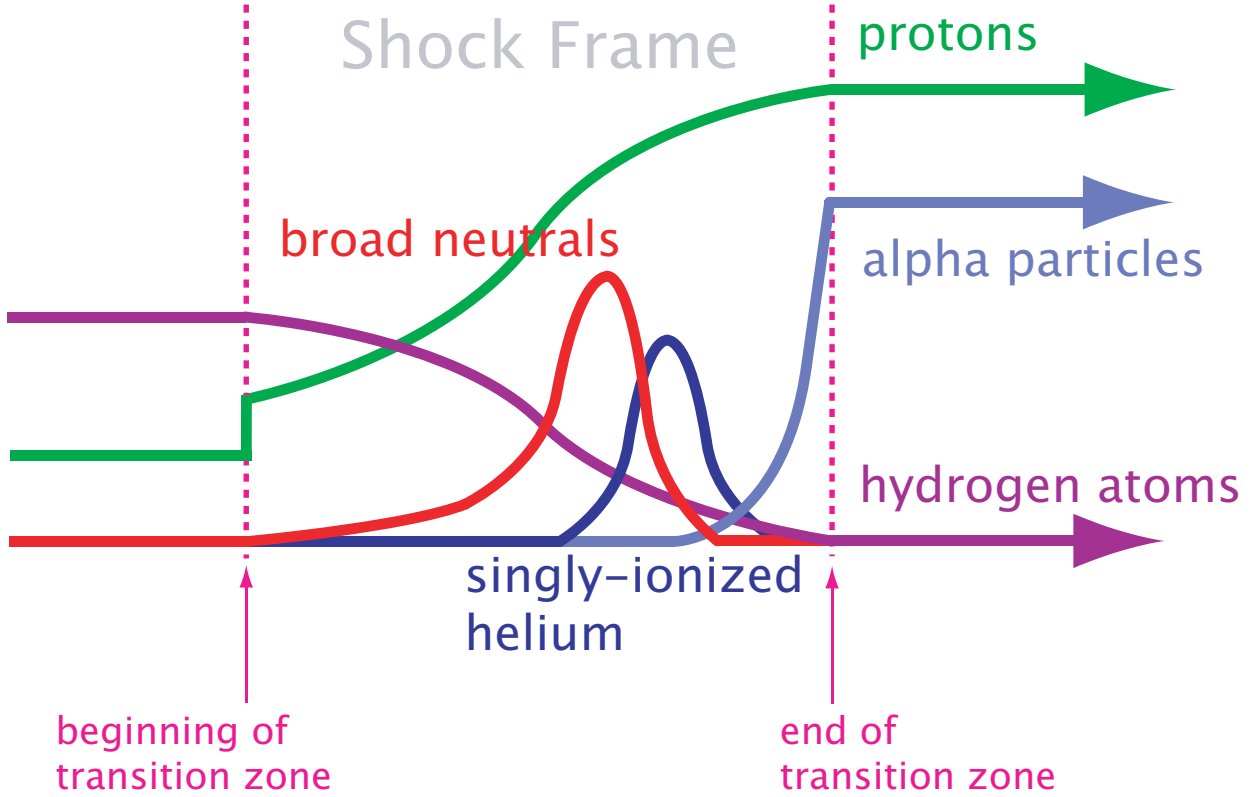


Fig. 1.— Schematic depiction of density variation in the shock transition zone. The vertical axis represents dimensionless density for the different particles species, while the horizontal axis represents distance. The shock front is marked by the left dotted vertical line. Upstream of the shock, negligible interactions take place between the particles. After protons and electrons are isotropized and decelerated at the shock front, ionization and charge transfer reactions deplete the cold neutrals and produce hot broad atoms. The transition zone terminates where all the neutral species are ionized, leaving a mix of protons, electrons and alpha particles.

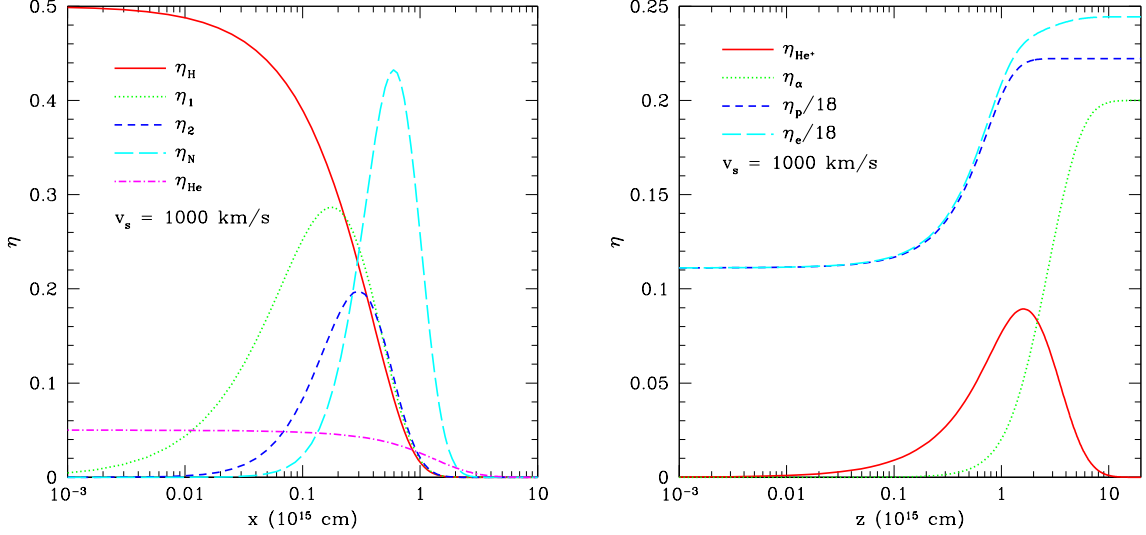


Fig. 2.— Dimensionless density as a function of physical distance behind the shock front, for parameters $v_s = 1000$ km s $^{-1}$, $f_p = 0.5$, $\beta = 1$, $n_0 = 1$ cm $^{-3}$, $f_{He} = 0.1$, and $d = 1$ kpc. The left panel shows the shock transition zone structure for the neutral species; the solid and dash-dotted curves show the density of neutral hydrogen and helium, respectively. Charge transfer reactions produce broad neutrals which have undergone one (dotted curve), two (short-dashed) and three or more (long-dashed) charge transfer reactions. The right panel shows the transition zone structure for the charged species. Note that the densities of the protons and electrons have been scaled by a factor of 1/18. Singly-ionized helium (solid curve) is produced downstream from the shock and ionized to produce alpha particles (dotted curve). The proton (short-dashed curve) and electron (long-dashed curve) densities saturate when the neutral species are fully ionized.

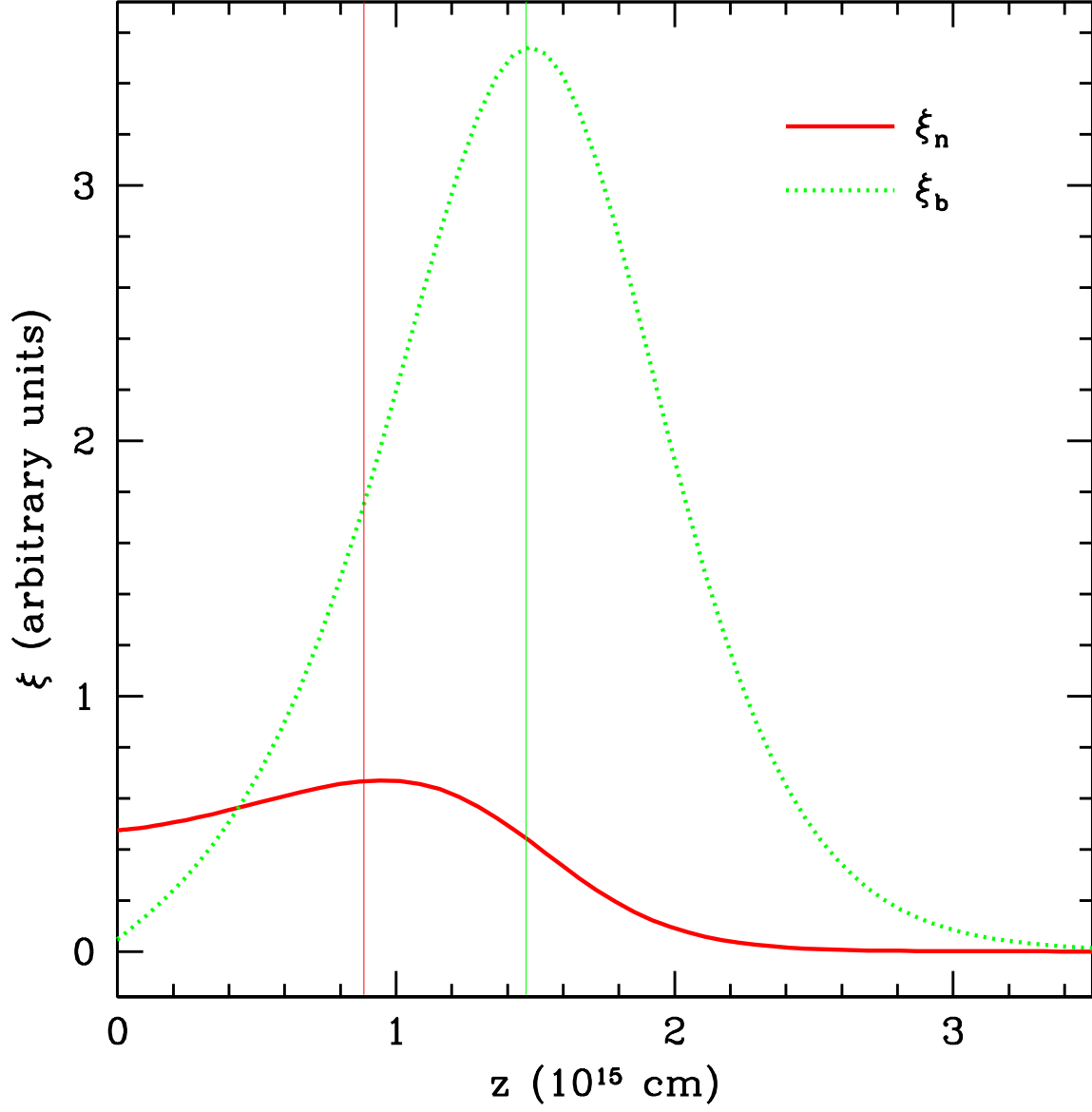


Fig. 3.— Emissivity profiles for narrow and broad emission as a function of distance behind the shock front. Results are shown for $v_s = 1000 \text{ km s}^{-1}$, $f_p = 0.1$, $\beta = 1$, and $f_{\text{He}} = 0.1$. The centroids of the narrow and broad profiles are indicated by the light vertical lines.

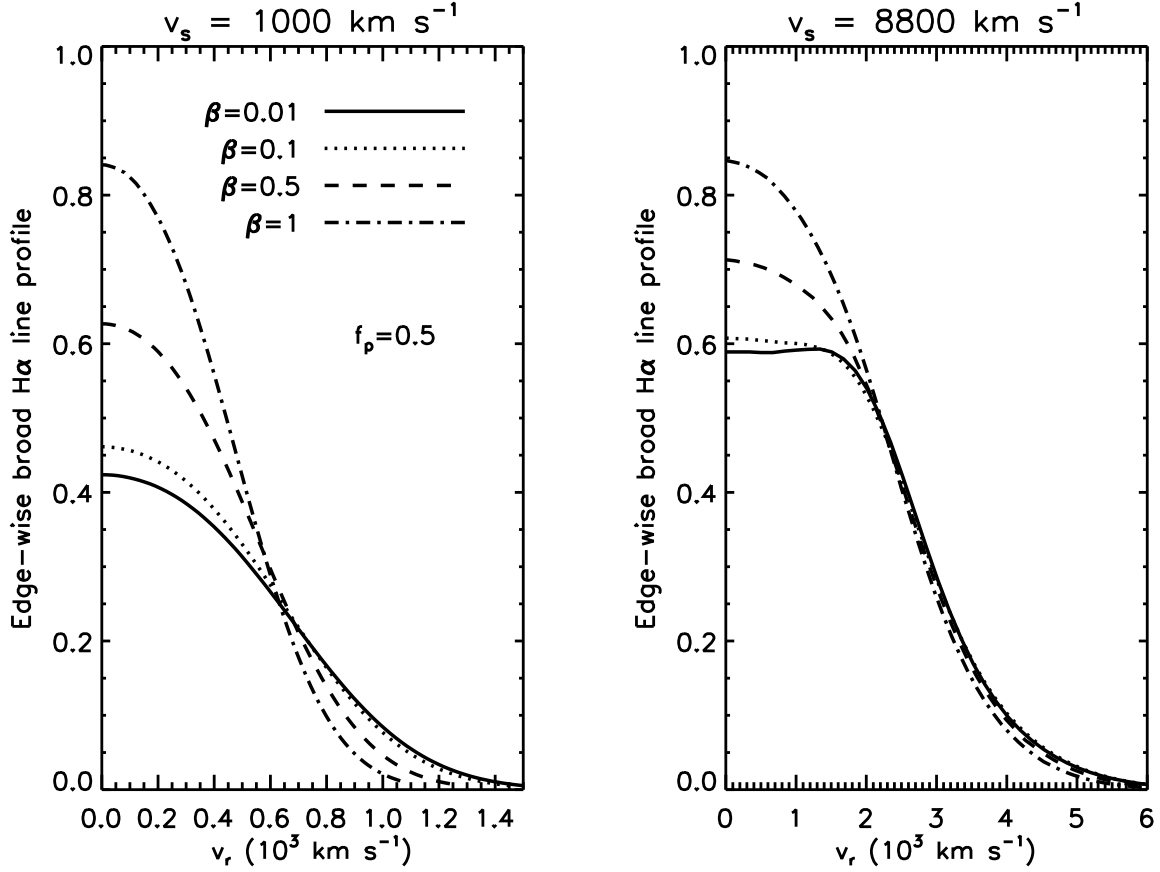


Fig. 4.— Symmetric, edge-wise H α line profiles as a function of line-of-sight velocity v_r , in a reference frame where the proton velocity is zero. Results are shown for fixed $f_p = 0.5$ and several values of $\beta = 0.01, 0.1, 0.5, 1$. As β is increased, the temperatures of the proton and broad neutral distribution functions decrease, leading to smaller FWHM.

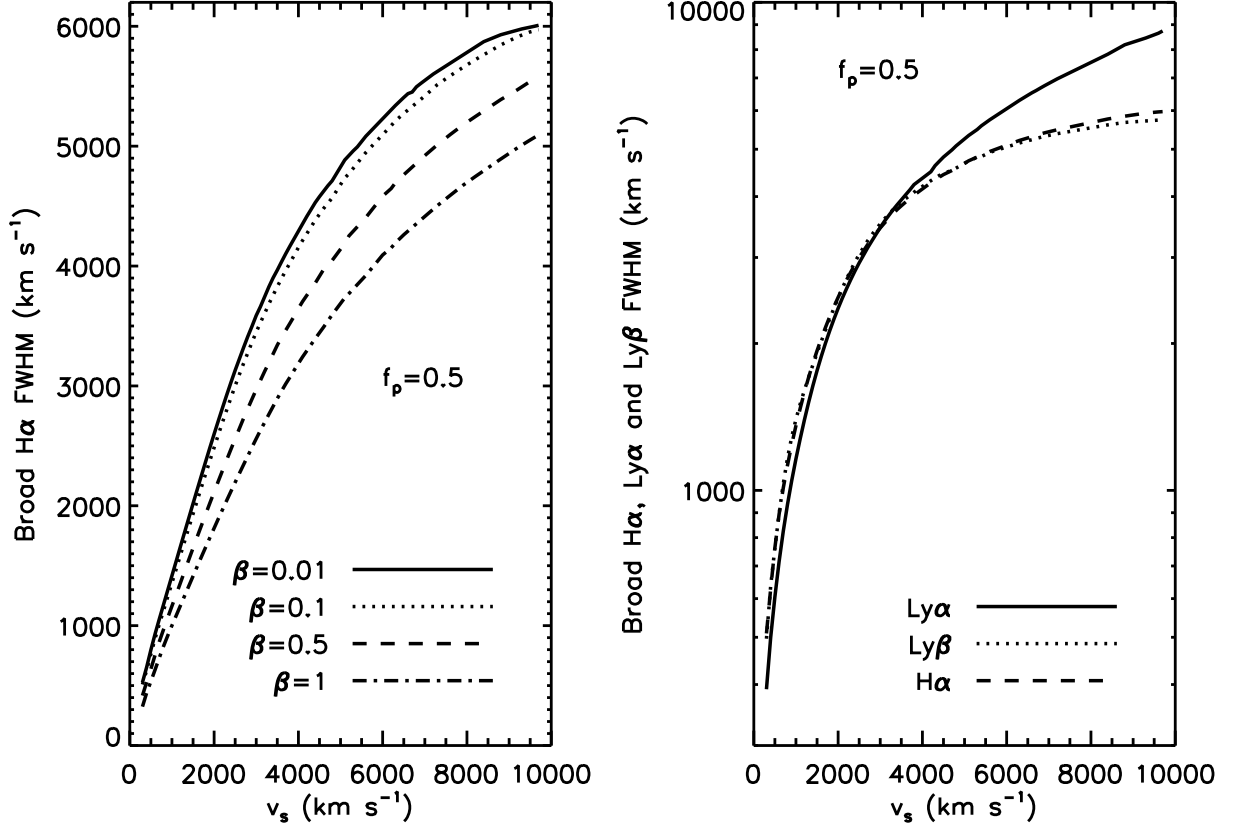


Fig. 5.— Broad line FWHM as a function of shock velocity for fixed f_p at several values of $\beta = 0.01, 0.1, 0.5, 1$ for H α (left panel), and fixed $\beta = 0.1$ for Ly α and Ly β (right panel). As β is increased, the predicted FWHM decreases (see Figure 4). It should be noted that at $v_s \gtrsim 4000$ km s $^{-1}$, our calculation predicts a larger width for the Ly α compared to H α broad component.

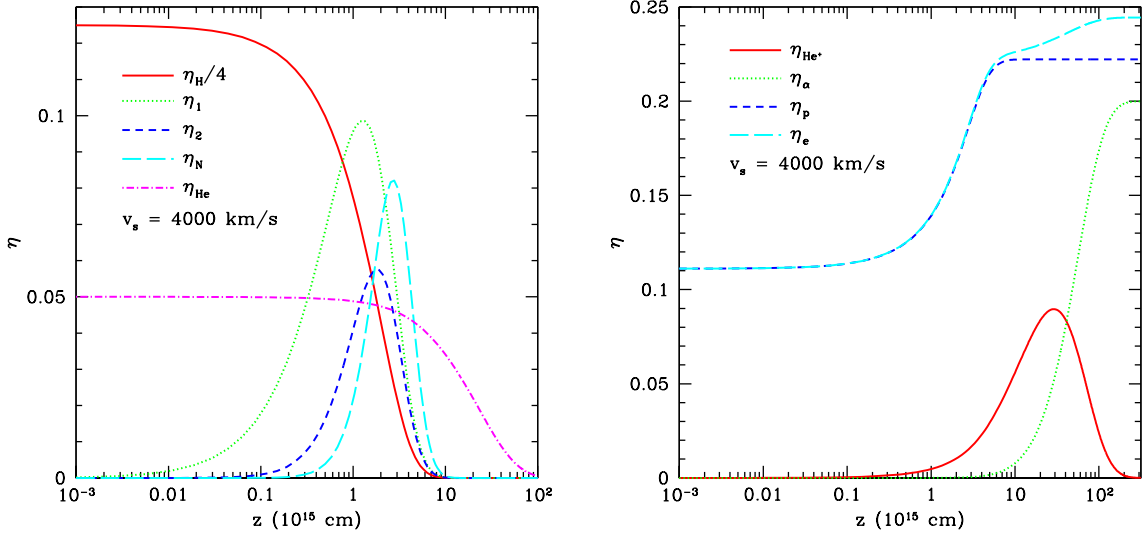


Fig. 6.— Same as Figure 2 except that $v_s = 4000$ km s $^{-1}$. The density of the hydrogen beam is scaled by $1/4$.

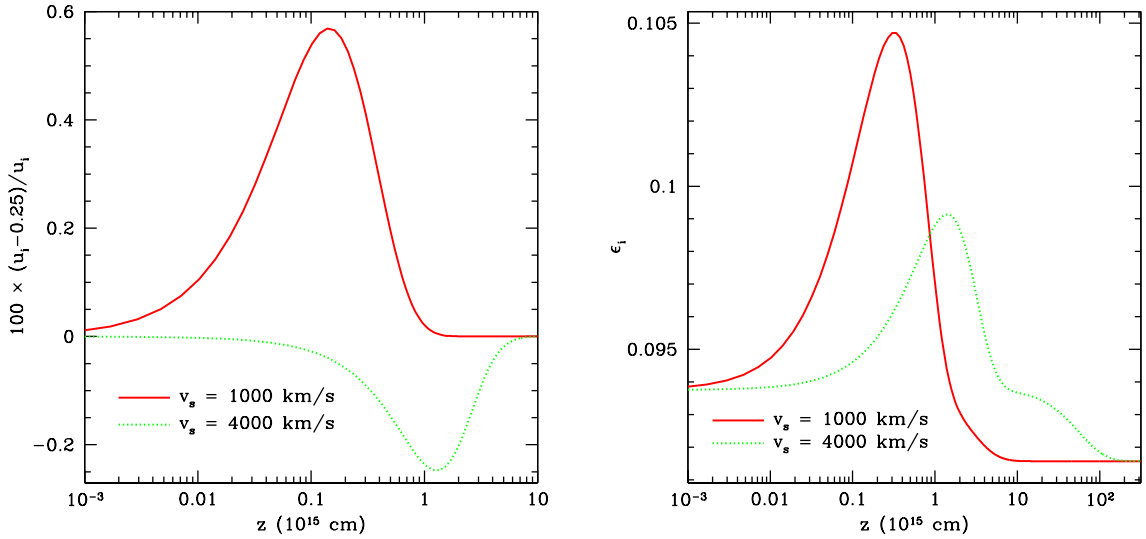


Fig. 7.— Percent deviation of the ion velocity from $v_s/4$ (left panel) and the ion temperature (right panel) as a function of position behind the shock front for two values of the shock velocity, $v_s = 1000$ km s $^{-1}$ (solid curve) and $v_s = 4000$ km s $^{-1}$ (dotted curve). Results are shown for $f_p = 0.5$, $\beta = 1$, and $f_{He} = 0.1$.

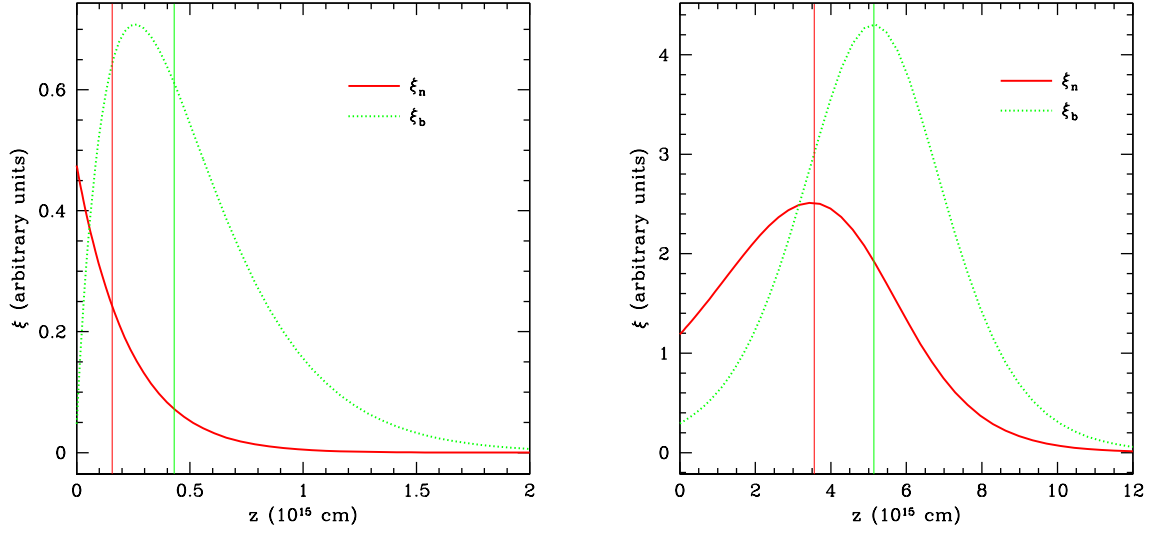


Fig. 8.— Same as Figure 3, except that $f_p = 0.9$, $v_s = 1000 \text{ km s}^{-1}$ (left panel) and $f_p = 0.1$, $v_s = 4000 \text{ km s}^{-1}$ (right panel).

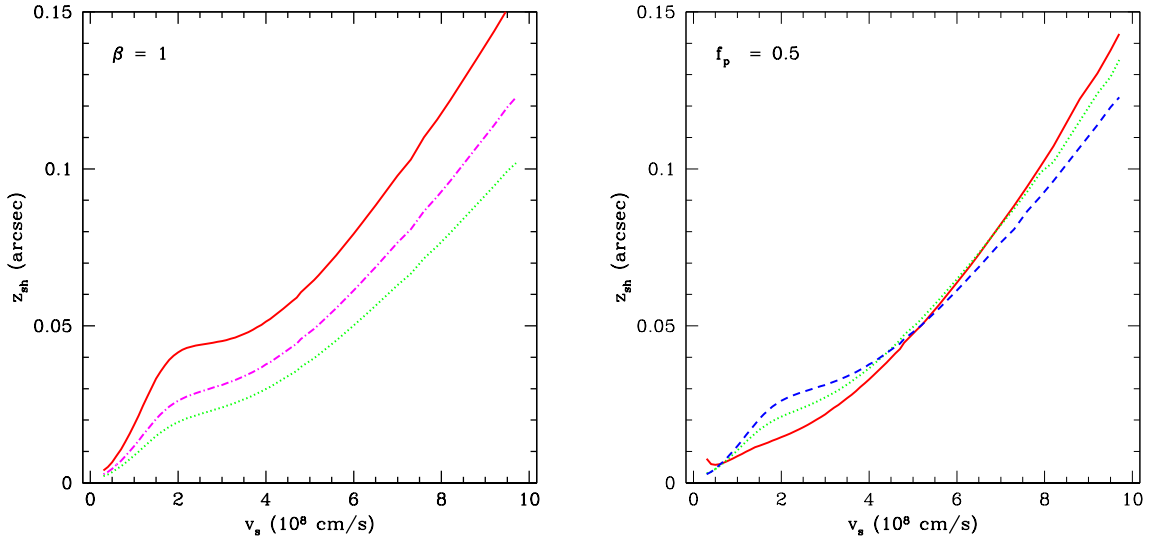


Fig. 9.— Spatial shift in units of 10^{15} cm as a function of shock velocity v_s . The left panel shows the variation of the shift with f_p at fixed $\beta = 1$. From top to bottom, the curves show results for pre-shock ionization fractions $f_p = 0.1, 0.5, 0.9$. The right panel shows the variation of the shift with β , for fixed $f_p = 0.5$. From bottom to top on the far left, the curves show results for temperature equilibration ratios $\beta = 0.1, 0.5, 1$.

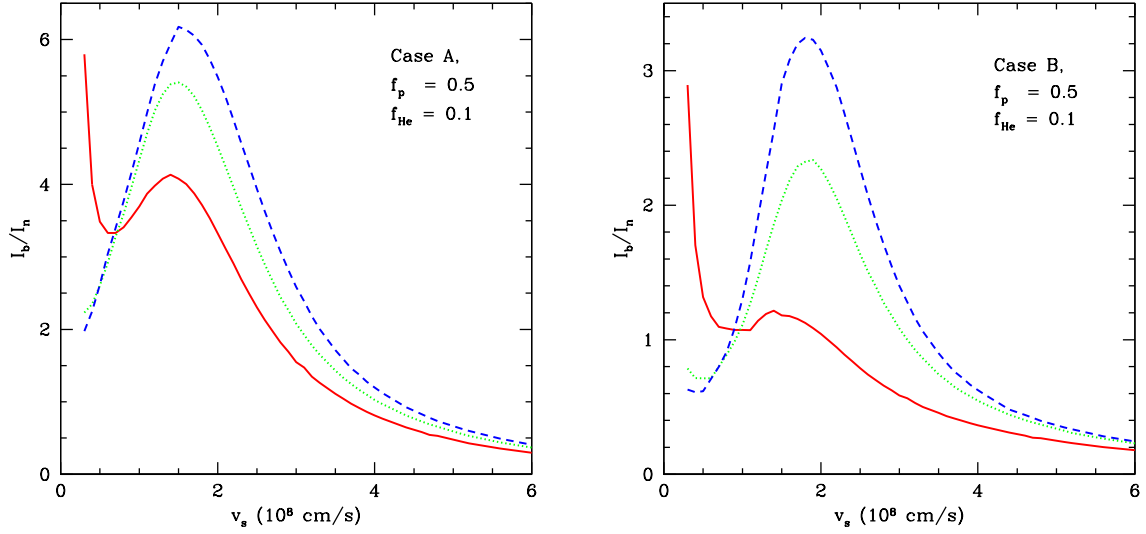


Fig. 10.— Broad to narrow intensity ratio I_b/I_n as a function of shock velocity v_s with $f_p = 0.5$, $f_{\text{He}} = 0.1$ for Case A (left panel) and Case B (right panel) conditions. From bottom to top, the curves show results for temperature equilibration ratios $\beta = 0.1, 0.5, 1$.

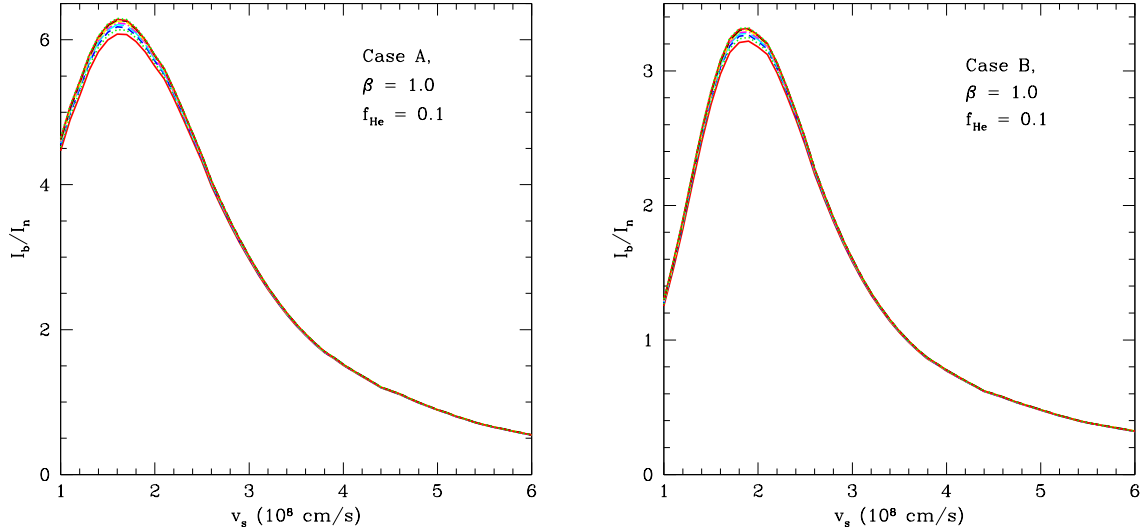


Fig. 11.— Broad to narrow intensity ratio I_b/I_n as a function of shock velocity v_s , with $\beta = 1$, $f_{\text{He}} = 0.1$, Case A (left panel) and Case B (right panel) conditions. From bottom to top, the curves show results for pre-shock ionization fraction $f_p = 0.1, 0.5, 0.9$.

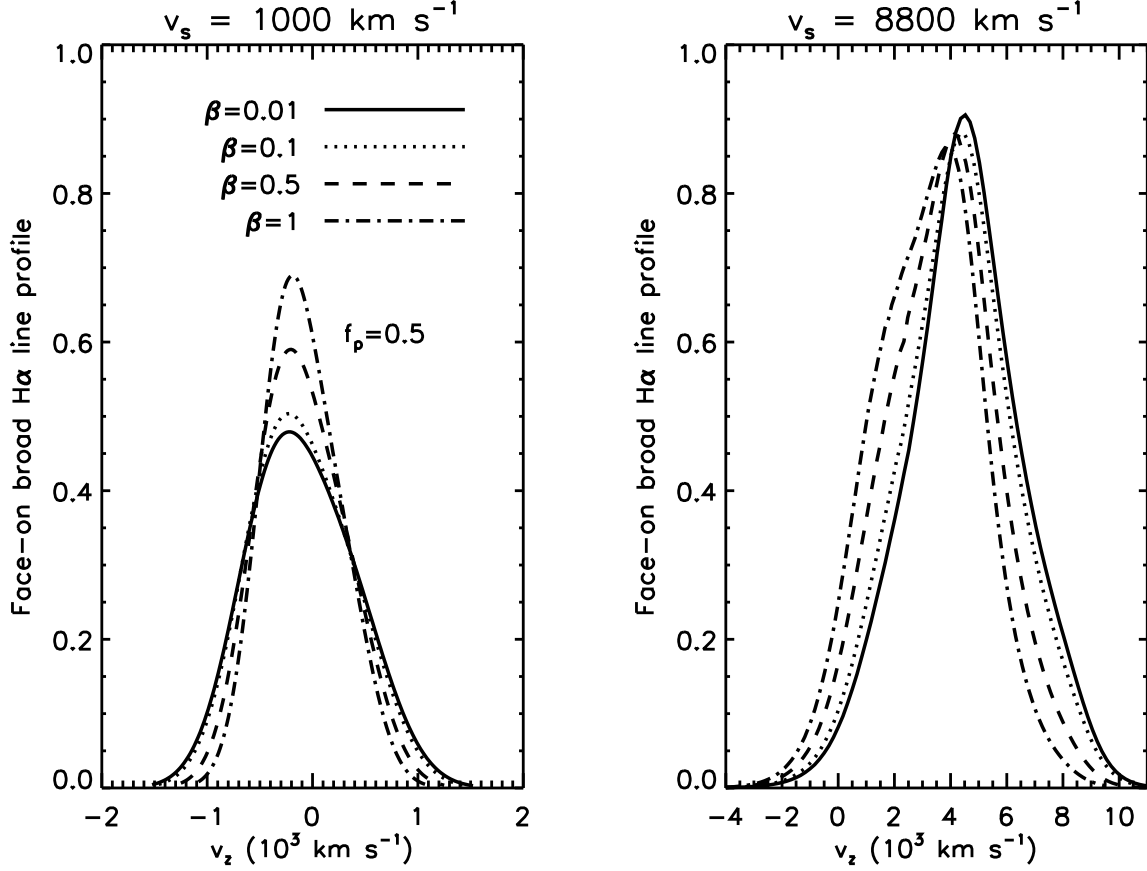


Fig. 12.— Face-on H α line profiles as a function of line-of-sight velocity v_z , in a reference frame where the proton velocity is zero. Results are shown for fixed $f_p = 0.5$, several values of $\beta = 0.01, 0.1, 0.5, 1$, at shock velocities $v_s = 1000$ km s $^{-1}$ (left panel) and $v_s = 8800$ km s $^{-1}$. At low shock velocity, charge transfer is extremely efficient, and the broad neutral distributions are very close to the thermal proton distribution (left panel). At high shock velocity, the broad neutral distribution function is skewed and offset from that of the protons, leading to the asymmetric velocity profiles depicted in the right panel.

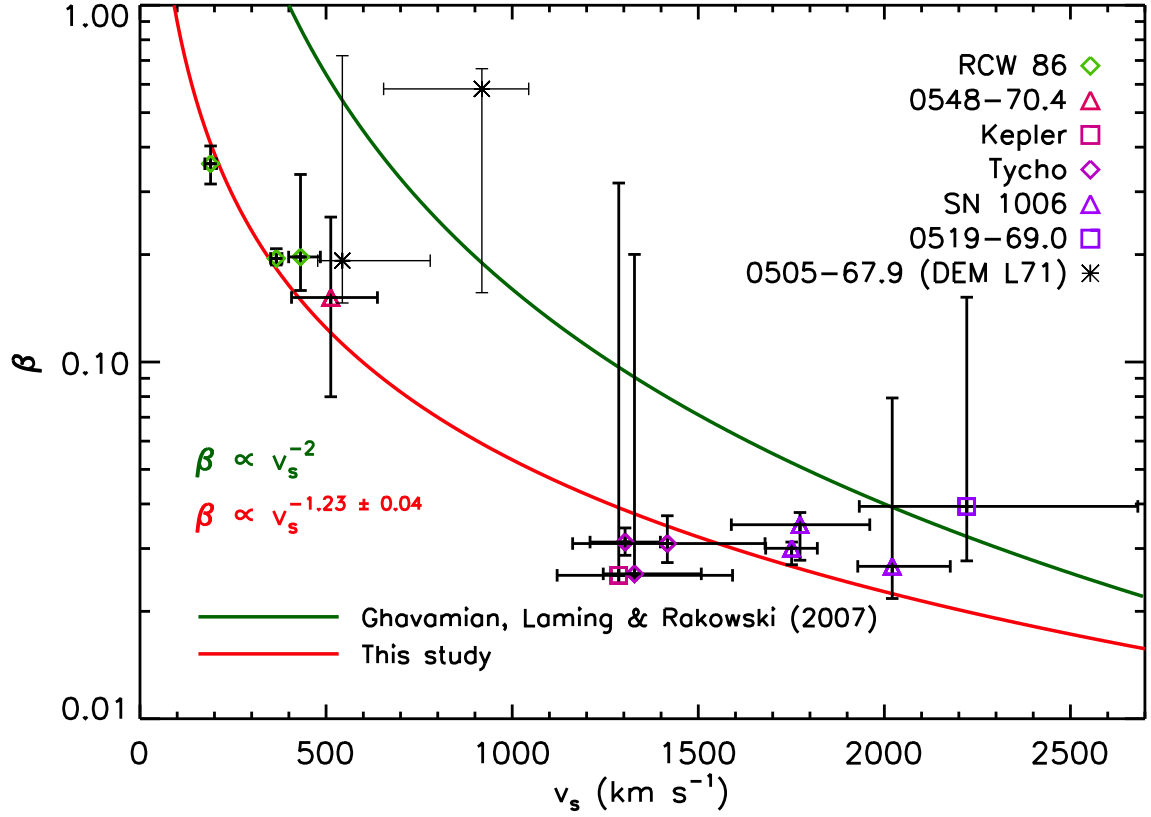


Fig. 13.— Temperature equilibration ratio β as a function of shock velocity v_s for Balmer-dominated shocks fit by our calculations. The symbol shape denotes the origin of the data point from SNRs in our sample. The bottom curve shows our best power-law fit $\beta \propto v_s^{-\alpha}$ to the observations, with $\alpha = 1.23 \pm 0.04$ and $\chi_r^2 = 16/10 = 1.6$. The top curve shows the relation from Ghavamian et al. (2007b). According to our calculation, the observations cannot be fit by $\beta \propto v_s^{-2}$, and may be consistent with two distinct regimes at low and high shock velocity. We conclude that electrons achieve higher temperatures at larger shock velocities. The previous result by Ghavamian et al. (2007b), in which electrons are heated to the same temperature independent of shock velocity, was largely based on inferences from objects which are not correctly described by non-radiative Balmer-dominated shock models (see §6.2 of the text).

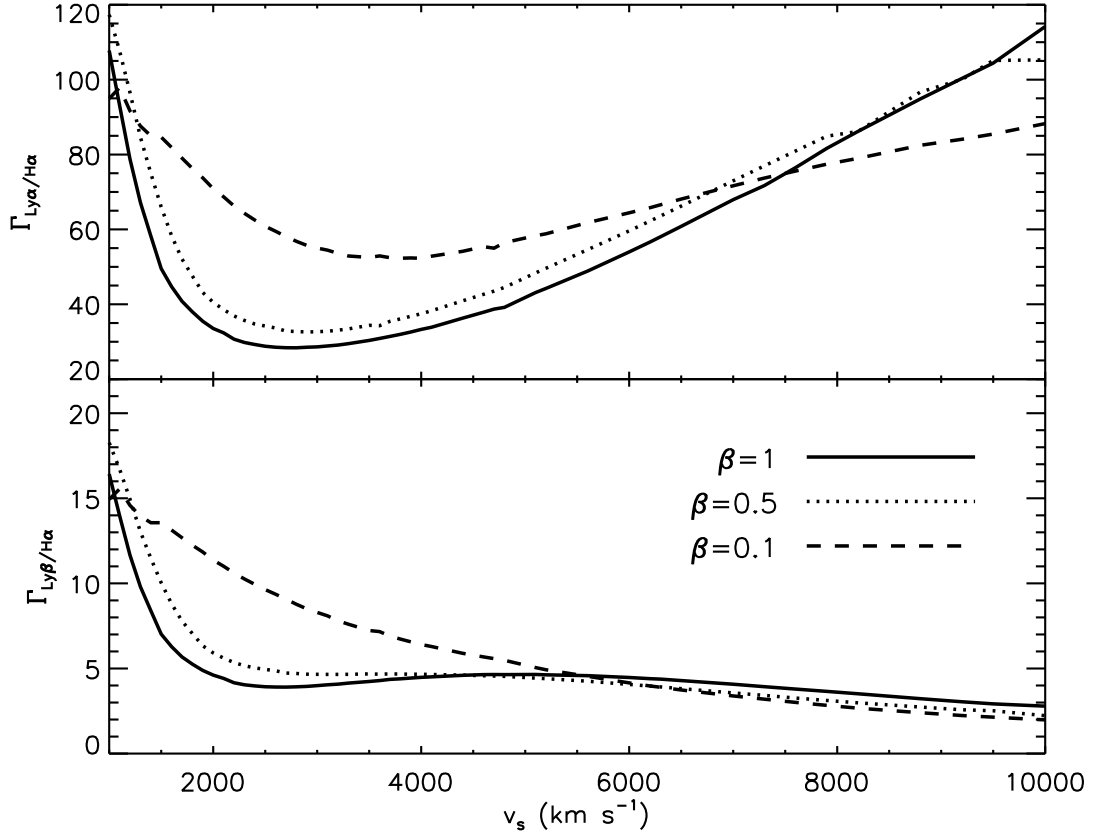


Fig. 14.— Luminosity ratios of broad $\text{Ly}\alpha$ and $\text{Ly}\beta$ to $\text{H}\alpha$, denoted $\Gamma_{\text{Ly}\alpha}/\text{H}\alpha$ and $\Gamma_{\text{Ly}\beta}/\text{H}\alpha$, respectively.

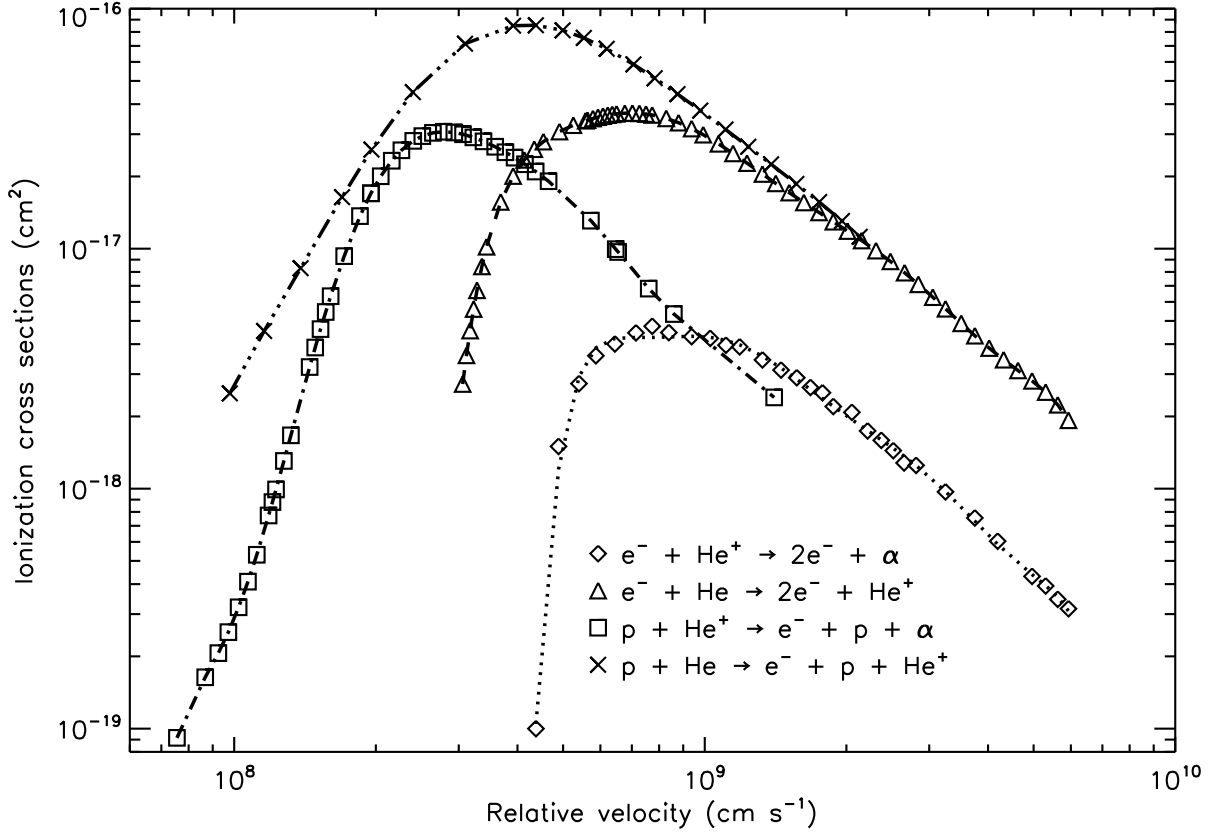


Fig. 15.— Cross sections for ionization of neutral and singly-ionized helium by electrons and protons. For references to the atomic data, see Appendix A.